Evaluating particle-suspension reactor designs for Z-scheme solar water splitting via transport and kinetic modeling — Source link ↗

Rohini Bala Chandran, Sasuke Breen, Yuanxun Shao, Shane Ardo ...+1 more authors

Institutions: Lawrence Berkeley National Laboratory, University of California, Irvine

Related papers:

- Recent advances in semiconductors for photocatalytic and photoelectrochemical water splitting

- Z-Scheme Water Splitting Using Two Different Semiconductor Photocatalysts

- Heterogeneous photocatalyst materials for water splitting

- Technical and economic feasibility of centralized facilities for solar hydrogen production via photocatalysis and photoelectrochemistry

- A comparative technoeconomic analysis of renewable hydrogen production using solar energy

Title

Evaluating particle-suspension reactor designs for Z-scheme solar water splitting via transport and kinetic modeling

Permalink

https://escholarship.org/uc/item/74d5g7sf

Journal

Energy and Environmental Science, 11(1)

ISSN

1754-5692

Authors

Bala Chandran, R
Breen, S
Shao, Y
et al.

Publication Date

2018

DOI

10.1039/c7ee01360d

Supplemental Material

https://escholarship.org/uc/item/74d5g7sf#supplemental

Peer reviewed

Evaluating Particle-Suspension Reactor Designs for Z-Scheme Solar Water Splitting via Transport and Kinetic Modeling

Rohini Bala Chandran,[1] Sasuke Breen,[2] Yuanxun Shao,[3] Shane Ardo,[2,3,*]
and Adam Z. Weber[1,*]

[1]Energy Technologies Area, Lawrence Berkeley National Laboratory, Berkeley, CA
94720, USA

[2]Department of Chemistry, University of California, Irvine, CA 92697-2025, USA

[3] Department of Chemical Engineering and Materials Science, University of California,
Irvine, CA 92697-2025, USA

*Corresponding authors. Email: ardo@uci.edu, AZWeber@lbl.gov

Broader Context

Pairing the most abundant energy resource on our planet, the Sun, with energy storage technologies is essential to overcome the diurnal variations in the availability of sunlight. Taking a *leaf* from plants, artificial photosynthetic devices capture and store sunlight in energy dense fuels by converting water and carbon dioxide to produce hydrogen and other hydrocarbons. For solar hydrogen production, particle-suspension reactor designs comprising suspended photocatalysts in an aqueous electrolyte are projected to be cost-efficient alternatives to the more exhaustively optimized fixed-electrode device architectures. However, there is a lack of a quantitative understanding of the device-scale transport and kinetic processes, and its impacts on the solar-to-hydrogen efficiencies for these designs. An innovative and intrinsically safe reactor design for Z-scheme solar water splitting is proposed. Two reaction compartments with suspended photocatalysts for hydrogen and oxygen production are optically connected in series to more efficiently utilize the incident solar spectrum while facilitating product separation. Soluble redox shuttles relay electrons between these compartments. A computational model is developed to guide device-design and operating conditions to achieve diffusion-sustained, efficient reactor operation. Results reveal the promise of using proton-coupled electron transport redox shuttles and the significance of selective surface catalysis of the redox shuttle to boost efficiency.

ABSTRACT

Sunlight-driven water splitting to produce hydrogen and oxygen provides a pathway to store available solar energy in the form of stable, energy-dense chemical bonds. Here we investigate a tandem particle-suspension reactor design for solar water splitting comprising micron-scale photocatalyst particles suspended in an aqueous solution with soluble redox shuttles. A porous separator facilitates redox species transport between the hydrogen and oxygen evolution reaction compartments while averting gas crossover. A two-dimensional, transient model of the reactor is presented to illustrate the coupling between light absorption, interfacial electron-transfer kinetics and species transport, and their combined impacts on overall solar-to-hydrogen conversion efficiency. The volumetric reactivity of the suspended semiconductor particles is dictated by combining the (photo)current–voltage behavior of a photodiode with Butler–Volmer electron-transfer kinetics. For the first time, a quantitative approach to determine the impacts of surface-dependent redox shuttle kinetic parameters on reaction selectivity in a Z-scheme system is established. Model results provide insights on the effects of optical, transport and kinetic properties of the semiconductor particles and the redox shuttles on the overall reactor performance. Solar-to-hydrogen reactor efficiencies predicted with $BiVO_4$ particles for oxygen evolution are at least two times larger than efficiencies achieved with wider band-gap TiO_2 particles due to enhanced visible light absorption; hydrogen evolution with $SrTiO_3$:Rh particles was considered for both cases. Superior performance is predicted with proton-coupled electron transfer redox shuttles (*para*-benzoquinone/hydroquinone and iodide/iodate) that absorb little-to-no visible light, while also facilitating operation at near-neutral pH conditions, as compared to the non-proton-

coupled triiodide/iodide and iron(III)/iron(II) redox shuttles. For 1 cm tall reaction compartments, diffusive species transport is fast enough to sustain reactor operation at a 1% solar-to-hydrogen conversion efficiency for both *para*-benzoquinone/hydroquinone and iodide/iodate redox shuttles with less than 2.2 mg L^{-1} of each of $BiVO_4$ and $SrTiO_3$:Rh particles in the solution.

INTRODUCTION

Stable, scalable and efficient devices for artificial photosynthesis offer the potential to harness and directly store the Earth's most abundant renewable energy resource in the form of energy-dense chemical bonds, such as those in hydrogen and hydrocarbons derived from carbon dioxide [1–3]. These solar fuels are net-carbon-neutral/negative alternatives to fossil fuels (assuming that the carbon is derived from combustion processes or the atmosphere), and enable storage and transport of solar energy for use when and where it is needed. Several solutions are being pursued for solar fuels production including photovoltaic-powered electrochemical devices for water and carbon dioxide splitting [4–7], solar thermochemical cycles [8–10], integrated photoelectrochemical (PEC) devices [11–16], and suspended photocatalyst particles [17–20]. Fixed-electrode, wafer-based PEC devices to split water, that consist of photoactive electrodes immersed in an aqueous electrolyte, have been experimentally demonstrated [12,21–26] and modeled extensively [27–34]. These designs have exhibited solar-to-hydrogen energy-conversion (STH) efficiencies as high as 18% [25] at 1 sun illumination and over 30% [26] with concentrated sunlight; however, these demonstrations suffered from stability issues where operational lifetimes were less than one day [12]. Recent technoeconomic analyses [35–37] make evident the need for fixed-electrode PEC devices to be operated at STH efficiencies greater than 25% to reach price parity with hydrogen produced from fossil fuels. However, the electrode-based devices that were stable for at least one day have exhibited STH efficiencies of at best 2% and they utilized designs that were inherently unsafe due to the generation of an explosive mixture of the H_2 and O_2 reaction products [20,38,39]. Reactor designs based on photocatalyst particle

5

suspensions [20] coupled with stable, low-cost and efficient material options are conceived to be cost-competitive with hydrogen produced from fossil sources, even at lower STH efficiencies of ~10%. The projected low levelized cost of hydrogen generated from particle-suspension reactors combined with the lack of in-depth knowledge for performance optimization of these reactors motivates the present study.

Numerous experimental demonstrations pertinent to particle-suspension, Z-scheme reactors with electron transfer mediated by a soluble redox shuttle have been reported [40–50], and a comprehensive review on this topic has been presented by Fabian and colleagues [20]. The predominant focus in the aforementioned studies was the identification of semiconductor materials [40–48] with enhanced activities for implementing the oxygen evolution reaction (OER) and the hydrogen evolution reaction (HER), development of surface treatment techniques and selection of redox shuttles to suppress undesired interfacial electron-transfer reactions [41,49], and evaluation of the effectiveness of cocatalyst [50] and coating materials [51]. In prior work, device-scale design and performance dependences on the transport and kinetic processes of the system were not considered. Therefore, from the standpoint of designing particle-suspension reactors, there is a need for a more holistic understanding of the intertwined multiphysics processes of light absorption, species transport in the electrolyte, and heterogeneous surface reactions to maximize the STH efficiency. Moreover, the implications of the kinetic parameters of the redox shuttle on the desired reaction rate have not been discussed in the previous studies.

Prior numerical models for solar water and carbon dioxide splitting have mostly been developed to guide the design of the fixed-electrode PEC devices [27–34]. Jaini and

6

Fuller [52] evaluated mass-transfer correlations for gas-induced convective mixing in a dual-bed, particle-suspension reactor and determined the steady-state redox shuttle concentration profiles assuming spatially homogenous reaction rates. However, the effects of optical absorption by the particles and the influence of interfacial electron-transfer kinetics on the species mass transport were absent from that study. For applications of water treatment with colloidal suspensions of TiO_2, volumetric light absorption and scattering properties of the suspension have been determined [53–55], and mass-transport limitations [56] and radiative transport [57] evaluated using numerical and experimental techniques. However, the target chemical reactions for water treatment are inherently different from water splitting, primarily because the overall reactions are often thermodynamically favorable, and tandem photosystems with soluble redox shuttles have not been considered for these applications.

In this paper, we report on the development of a transient, two-dimensional numerical model of a vertically stacked, Z-scheme particle-suspension reactor for sunlight-driven water splitting. This design (Figure 1) includes two important advances from prior conceptual designs for dual-bed Z-scheme reactors. The vertical arrangement of the reaction compartments facilitates tandem light absorption, which results in increased theoretical maximum STH efficiencies. By stacking the compartments, this design can afford mass transport over the smallest possible distances, therefore enabling sustained (effectively indefinite) reactor operation *in the absence of convection.* A notable advantage of the proposed Z-scheme reactor design is the opportunity to evolve H_2 and O_2 in separate physical locations, thus preventing formation of an explosive mixture of gases. The model developed accounts for diurnal variations in the incident
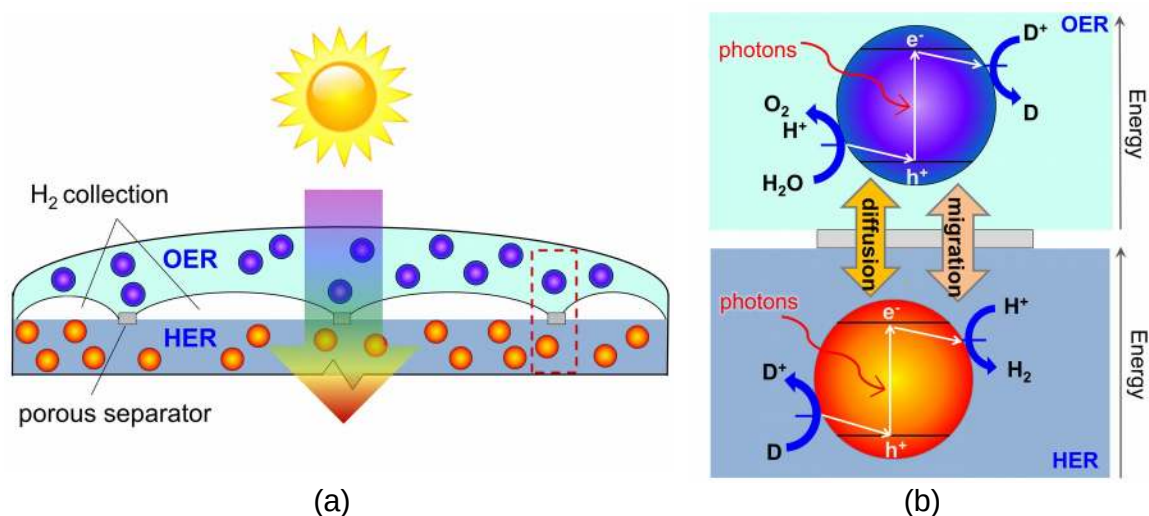
Figure 1. (a) Schematic of the vertically stacked particle-suspension reactor design which affords tandem light absorption for Z-scheme solar water splitting, and (b) the desired chemistry and direction of the electron transfer reactions on the surface of the semiconductor particles, assuming acidic conditions. D$^+$/D is only used to represent symbolically a redox shuttle and the respective counterions are not shown.

Oxygen evolution reaction (OER) particles	$+¿+\frac{1}{2}O_2+2D$ $+¿\rightarrow 2H^¿$ $H_2O+2h\nu+2D^¿$		(L1)
	$+¿+\frac{1}{2}O_2$ $+¿\rightarrow 2H^¿$ $H_2O+2h^¿$ (OER)	$-¿\rightarrow 2D$ $+¿+2e^¿$ $2D^¿$ (R$_{red}$)	
Hydrogen evolution reaction (HER) particles	$+¿+2h\nu+2D\rightarrow H_2+2D$ $2H^¿$		(L2)
	$+¿$ $+¿\rightarrow 2D^¿$ $2D+2h^¿$ (R$_{ox}$)	$-¿\rightarrow H_2$ $+¿+2e^¿$ $2H^¿$ (HER)	
Net	$H_2O+4h\nu\rightarrow H_2+\frac{1}{2}O_2$		(WS)

solar irradiation and couples the effects of optical absorption in the aqueous suspension, power supply of an ideal photodiode, reversible interfacial reaction kinetics, and species mass transport. By varying reactor height, and concentrations of the semiconductor

8

particles and the redox shuttle species the model is used to evaluate transient reactor performance and identifies STH efficiencies that maintain sustained reactor operation.

PARTICLE-SUSPENSION REACTOR

Our study specifically considers a tandem particle-suspension reactor for solar water splitting that relies on a two-step Z-scheme mechanism [58] and a reversible redox shuttle dissolved in an aqueous electrolyte (Figure 1). In a Z-scheme mechanism, the thermodynamic energy requirement for water splitting (WS) is attained using two photosystems (L1 and L2), similar to natural photosynthesis. Absorption of solar photons by a particle results in both an anodic (OER and R_{ox}) and a cathodic (HER or R_{red}) half-reaction being driven at distinct semiconductor–electrocatalyst–electrolyte interfaces. Figure 1 shows OER and R_{ox} in the top compartment, and HER and R_{red} in the bottom compartment, but this is not a necessity for the design and the choice of the redox shuttle determines which reactions should optimally be driven in the top and bottom compartments. Electrocatalyst deposited on semiconductor surfaces is commonly referred to as a cocatalyst in the pertinent literature [20], and we adopt this terminology in the rest of this paper. As shown in Figure 1, in the top compartment, light absorption generates holes that oxidize water to O_2 (OER) and electrons that reduce the oxidized state of the redox shuttle, $D^+ \rightarrow D$ (R_{red}). In the bottom compartment, light absorption generates electrons that reduce protons to H_2 (HER), while simultaneously the photo-generated holes regenerate the oxidized state of the redox shuttle, $D \rightarrow D^+$ (R_{ox}). Cocatalysts deposited on these particles reduce overpotentials for the desired redox reactions and potentially also improve the product selectivity for the desired pair of surface reactions (OER and R_{rd}; HER and R_{ox}) by influencing the charge-separation and electron transfer

9

mechanisms. Intrinsic separation of product gases makes this design safe, and reduces Faradaic losses and explosion hazards that can occur due to reactions between product gases.

The ability of a particle-suspension reactor to attain large STH efficiencies and demonstrate sustainable operation relies in part on effective mass transport of the redox shuttle (D^+/D) and protons, or hydroxides under alkaline conditions, between the physical locations of the particles for effecting the HER and the OER [20]. In the proposed reactor design, the characteristic lengthscale for diffusive mass transport and incident light absorption is the reaction compartment height. To maximize the rate of photon absorption and minimize energy losses associated with large concentration gradients, the reaction compartment height therefore needs to be optimized. The mass-transport lengthscales considered here are on the order of centimeters, in contrast to the mass-transport lengthscales on the order of meters for horizontally-adjacent dual-bed designs [35,36].

After surveying the semiconductor materials, dopants, cocatalysts, and redox shuttles reported in the literature [20], we selected semiconductor materials with demonstrated stability as aqueous suspensions, appropriate band energies to drive the desired reactions, and availability of published data on optical properties. Two options were investigated for the OER semiconductor materials: Option I, which benefited from use of semiconductor particles with complementary bandgaps, and Option II, which did not (Table 1). For Option I, the OER material was TiO_2 (E_{bg} = 3.1 eV[59], average value of its two most common crystal structures) and for Option II the OER material was $BiVO_4$ (E_{bg} = 2.5 eV) [20,60], both materials with high reported activities for the light-driven OER in Z-scheme designs [41,49,50,61]. The HER material for both these

options was rhodium-doped $SrTiO_3$, with a lowest-energy absorption onset of 2.5 eV, due

to

Table 1. Semiconductor materials and redox shuttles for model simulations

	Option I	Option II
Semiconductor materials	**OER — TiO_2** [59,71] E_{bg} = 3.1 eV	**OER — $BiVO_4$** [20,60] E_{bg} = 2.5 eV
	HER — $SrTiO_3$:Rh [62,72,73] E_{bg} = 2.5 eV	
Redox shuttles (D^+/D)	I_3^-/I^- (pH < 4) [41], Fe^{3+}/Fe^{2+} (pH < 2.5) [50], IO_3^-/I^- (pH > 7) [41], Q/QH_2 (acidic to neutral) [74,75]	

excitation from a Rh^{3+} defect band to the $SrTiO_3$ conduction band [62], and one-of-the-

best reported activities for the light-driven HER in Z-scheme designs [45,48,51]. Table 1

shows the band gaps of the selected photocatalysts, which have suitable band-edge

positions for the valence and conduction bands (denoted by E_{vb} and E_{cb} in Table 2)

relative to the desired redox reaction potentials. To mediate charge transport across the

solutions, various demonstrated redox shuttles were analyzed (I^-/I_3^-, I^-/IO_3^- [20,41,42,49]

and Fe^{3+}/Fe^{2+} [48,50,63]) as well as an organic redox couple, *p*-

benzoquinone/hydroquinone (Q/QH_2), which has been used in state-of-the-art aqueous

redox flow batteries and can undergo proton-coupled electron transfer redox

chemistry[64–66]. Table 1 shows the pH conditions required for each redox shuttle to

maintain it as the dominant species in solution. Acidic conditions (pH < 4) are required

for the I_3^-/I^- and the Fe^{3+}/Fe^{2+} redox shuttles; for the Fe^{3+}/Fe^{2+} redox shuttle, a one-

electron-transfer reaction was analyzed. By coupling the proton-coupled electron transfer

reactions for Q/QH_2 with the inherently proton-coupled-electron-transfer OER or HER

the overall reactions in each compartment exhibit pH independent thermodynamic potentials,

$$H_2O + 2h\nu + Q \rightarrow QH_2 + \frac{1}{2}O_2 \qquad\qquad E^0 = 0.53V$$

$$QH_2 + 2h\nu \rightarrow H_2 + Q \qquad\qquad E^0 = 0.7V$$

The IO_3^-/I^- redox shuttle also exhibits proton-coupled electron-transfer reactions (six proton, six electron-transfer reactions).

The interfacial reaction kinetics for the OER and the HER were modeled by considering the electron-transfer properties of state-of-the-art electrocatalysts, RuO_2 for OER [27,67,68] and Pt for HER [27,69,70], even though in practice these cocatalysts are not always used [20]. The choice of the photocatalyst and the cocatalyst (if present) will impact the overpotentials for each redox reaction and determine the reaction selectivity. Therefore, the impacts of the redox shuttle kinetic parameters (exchange current density, $j_{0,sh}$, and charge transfer coefficients, $\alpha_{a,sh}, \alpha_{c,sh}$) were examined in addition to the baseline simulations that assumed ideal selective catalysis with facile redox chemistry.

For each of these cases, the developed model was used to evaluate the effects of the reaction compartment heights (1 to 10 cm), and the concentrations of the semiconductor particles (10^{-6} to 1 g L^{-1}) and the redox shuttles (10^{-4} to 5 M) on achieving sustained reactor operation, aided by only diffusive species transport, for a baseline STH efficiency of 1%. This modest efficiency target is set to evaluate the theoretical feasibility of the reactor design. Pathways to achieve higher STH efficiencies with the proposed design are also reported.

THEORETICAL

Modeling Domain and Assumptions

A transient, two-dimensional, continuum transport model was developed to simulate light absorption and mass transport in the reactor. Figure 2 depicts the numerical modeling domain with the key governing equations used to model the coupled physical processes and the applied boundary conditions. Table 2 presents the baseline case modeling parameters. The domain comprises the two reaction compartments and a porous separator, and exploits centerline symmetry to reduce the computational expense. The aqueous suspension is assumed to contain a spatially homogeneous and continuous distribution of particles that remain completely soluble. The continuum transport equations formulated are hence applied for an "effective" medium comprising the suspended particles and the aqueous electrolyte. For colloidal suspensions with solid/particle volume fractions less than 0.006, the effective medium and independent light scattering are valid approximations [76]. These volume fractions translate to particle concentrations less than 20 g L^{-1}, 40 g L$^{-1,}$ and 30 g L^{-1} based on the bulk densities of TiO$_2$, BiVO$_4$, and SrTiO$_3$:Rh, respectively (listed in Table 2), and we consider concentrations below 5 g L^{-1} for the model simulations. Therefore, treating the suspension as an effective medium and assuming independent light scattering are reasonable approximations. The size of the particle, d_p, does not directly enter the analysis since the model treats the particles as point locations and thus assumes that the rates of charge-carrier transport (diffusion and migration) within the particle are much faster than the reaction rates and device-scale diffusive rates of species transport. This assumption is

reasonable considering that the particles considered here are much smaller relative to the

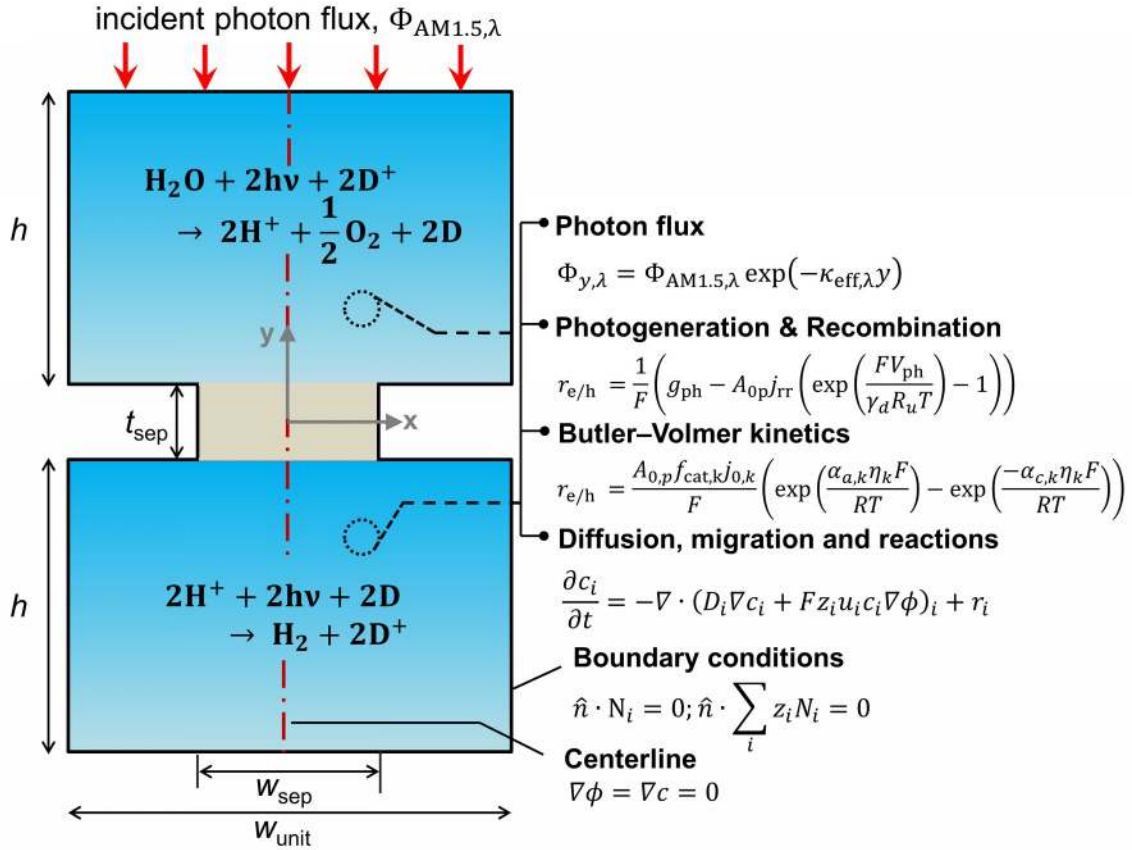device dimensions (d_p ~100 nm vs. h = 1 cm – 10 cm).

Figure 2. Schematic of the two-dimensional unit cell of the reactor (not drawn to scale). It lists the key geometric parameters and the governing equations modeled for evaluating coupled light absorption, reaction kinetics, and species transport in the reactor. The modeling domain comprises one-half of the unit cell and exploits centerline (red dashed line) symmetry; boundary conditions applied on its external boundaries (solid black lines) and the vertical centerline are shown.

Table 2. **Baseline values for the modeling parameters**

Category	Parameter (Unit)		Values
Geometric Parameters	t_{sep} (mm)		1
	w_{unit} (cm)		1
	$\dfrac{w_{sep}}{w_{unit}}$		0.8
	ε_{sep}		0.26
Semiconductor Particles	j_{rr} (A m^{-2})	TiO$_2$ and BiVO$_4$	10^{-18}
		SrTiO$_3$:Rh	10^{-15}
	E_{vb} (V *vs. NHE*) [20,59,62,71,73]	TiO$_2$	2.6
		BiVO$_4$	2.5
		SrTiO3:Rh	2
	E_{cb} (V *vs. NHE*) [20,59,62,71,73]	TiO$_2$	-0.5
		BiVO$_4$	-0.25
		SrTiO$_3$:Rh	-1
	ρ_p (g cm^{-3})	TiO$_2$	4.23
		BiVO$_4$	6.95
		SrTiO$_3$:Rh	4.81
	γ_d		1
	d_p (nm)		100
Redox shuttles and electrolytes	D_i [65,77] (10^{-9} m^2 s^{-1})	I$^-$, I$_3^-$, IO$_3^-$	2, 1, 1
		Fe^{3+}, Fe^{2+}	0.8, 0.8
		Q, QH$_2$	0.6, 0.74
		H$^+$	9.3
		K$^+$, Cl$^-$	2
	Aqueous solubility (M) [78]	KI, KIO$_3$	8.92, 0.43
		FeCl$_3$, FeCl$_2$	5.7, 5.2
		Q, QH$_2$	0.1, 0.5
	E^0 (V *vs. NHE*) [79]	I$^-$/I$_3^-$; I$^-$/ IO$_3^-$	0.536; 1.085
		Fe^{3+}/Fe^{2+}	0.771
		Q/QH$_2$	0.7
Kinetic Parameters	$j_{0,OER}$ (A m^{-2})	OER [27,67,68]	10^{-3}
	$\alpha_{a,OER}, \alpha_{c,HER}$		1, 0.1
	$j_{0,HER}$ (A m^{-2})	HER [27,69,70]	10
	$\alpha_{a,HER}, \alpha_{c,HER}$		2.56, 2.56
	f_{cat}		0.5

Porous Separator

The porous separator dimensions (t_{sep}, w_{sep}) and porosity, ε_{sep}, are selected to restrict diffusive gas crossover losses to less than 2%, a value that results in H_2 and O_2 streams with purity that is large enough to prevent formation of explosive mixtures [28]. The conditions for this safe operation were determined by applying a one-dimensional Fickian diffusion model assuming saturated dissolved gas concentrations (1.23 mM for H_2 and 0.78 mM for O_2). For a separator thickness (t_{sep}) of 1 mm, the following relation holds, $\dfrac{w_{sep}\varepsilon_{sep}}{w_{unit}} < 0.21$, where $\dfrac{w_{sep}\varepsilon_{sep}}{w_{unit}}$ is an "effective" porosity of the separator to minimize gas crossover. More details about this calculation are provided in the ESI. For the baseline case, the ratio of the separator width to the unit cell width, $\dfrac{w_{sep}}{w_{unit}}$, is arbitrarily chosen to be 0.8, yielding a required separator porosity, $\varepsilon_{sep} < ¿$ 0.26.

Conversion of Light to Power

The spatial profile of light intensity in the compartments depends on the effective optical properties (absorption and scattering) and can be approximated by the Beer—Bouguer—Lambert law for solutions with negligible scattering and radiative emission. Negligible radiative emission is a reasonable assumption at low operating temperatures, whereas scattering effects can be neglected only when particle/aggregate sizes are small (typically less than 10 nm) relative to the incident wavelengths of sunlight. For larger particles/aggregates, both absorption and scattering effects have to be taken into consideration to obtain the spatial distribution of photon fluxes [53,76], and therefore

reaction rates. However, in the absence of literature data to correlate the particle size –

optical property dependencies and the added complexities to solve the full radiative

transport equation, we applied Beer's law (eq.(1)) to evaluate the spatial profile of photon

flux Φ along the height of the reactor,

$$\Phi_{y,\lambda} = \Phi_{AM1.5,\lambda} \exp\left(-\kappa_{eff,\lambda} y\right) \tag{1}$$

where $\Phi_{AM1.5,\lambda}$ is the incident AM1.5G [80] photon flux and $\kappa_{eff,\lambda}$ is the effective

spectral absorption coefficient of the particle suspension. Applying Beer's law (eq.(1))

represents a worse-case scenario for the spatial gradients of the photon fluxes, and is

expected to overpredict light absorption in the suspension. The day/night variation in the

incident photon flux was obtained from the TMY3 database [81] and was scaled to the

AM 1.5G spectrum for the peak insolation month of July at Daggitt, which is located in

Southern California and was chosen for its prospects of large-scale photovoltaic and

concentrated solar power generation at this location. The semiconductor particles and the

chemical species in the electrolyte contribute to the effective absorption coefficient,

$$\kappa_{eff,\lambda} = \kappa_{p,\lambda} C_p + \sum_{i=1}^{i=N} \acute{\epsilon}_{i,\lambda} c_i \tag{2}$$

where $\kappa_{p,\lambda}$ is the mass-specific, spectral absorption cross-section of the suspended

semiconductor particles, C_p is the semiconductor particle concentration, and $\acute{\epsilon}_i$

and c_i are the molar absorption coefficient and concentration of the ith species in the

electrolyte, including water [82]. Figure S1 depicts the absorption coefficients of the

various semiconductor particles [48,83,84] and redox mediators [85–87] considered.

Optical attenuation of incident light by the cocatalysts and the porous separator are

neglected. This is a reasonable assumption because shading effects due to the cocatalysts

are anticipated to be small in particle-suspension reactor designs. Moreover, cocatalysts

are often used at far less than submonolayer coverages and are likely present in discontinuous patches in the suspension, and polymer materials suitable for the porous separator exhibit negligibly low absorbance values in the far ultraviolet–visible region of the electromagnetic spectrum (see Figure S2). Values for $\Phi_{\lambda, AM1.5}$ and $\kappa_{eff, \lambda}$ can also be used to calculate the photon-flux weighted absorption cross-section of the particle, $\acute{\kappa}_p$, and the optical thickness, τ_p (see eq. (3a)) . Optical thickness is a critical dimensionless parameter that is linearly dependent on the particle concentration, absorption cross-section of the particles, and optical path length, h. It is a dimensionless indicator of the amount of sunlight absorbed by the semiconductor particles. The photon-flux weighted absorption cross-section of the particle, $\acute{\kappa}_p$, is used to determine the particle optical thickness, due to wavelength dependent optical properties.

$$\tau_p = \acute{\kappa}_p C_p h \tag{3a}$$

$$\acute{\kappa}_p = \frac{\int\limits_{\lambda=0}^{\lambda=\lambda_{bg}} \Phi_{\lambda, AM1.5} \acute{\kappa}_{p,\lambda} d\lambda}{\int\limits_{\lambda=0}^{\lambda=\lambda_{bg}} \Phi_{\lambda, AM1.5} d\lambda} \tag{3b}$$

Larger optical thicknesses result in increased sunlight absorption, which can be obtained by increasing the particle concentration and/or absorption properties of the material and/or optical path length.   For simplicity, this weighted optical thickness is termed solely the "optical thickness" throughout the text. We chose this value over the photon-flux-weighted, spectrally-averaged percent of light absorbed (absorptance) because optical thickness is linear in both concentration of particles and reactor height, allowing for a more conceptual interpretation of the values. For reference, using 1 g L^{-1} of the

suspended particles, $h=1$ cm, the particle optical thicknesses are 54.5, 18.2 and 16.5 for TiO$_2$, BiVO$_4$ and SrTiO$_3$:Rh, respectively.

The ideal photodiode equation has been used in prior modeling of fixed-electrode PEC devices to describe the (photo)current–voltage behavior of rectifying semiconductor–electrolyte junctions [88,89]. While the photodiode equation may not be appropriate to describe the behavior of individual semiconductor particles whose photon absorption rate is low, we expect that the photodiode equation is appropriate to describe an ensemble of semiconductor particles in a suspension. Particle-suspension reactors effectively perform *volumetric* reactivity as compared to interfacial, *areal* reactivity in the fixed-electrode, wafer-based PEC geometries. Therefore, the flux of charge carriers transported across the semiconductor–electrolyte interface [89] was recast as a volumetric rate, $r_{e/h}$, to obtain the volumetric version of the ideal photodiode equation,

$$r_{e/h} = \frac{1}{F}\left(g_{ph} - A_{0p}\, j_{rr}\left(e^{\left(\frac{FV_{ph}}{\gamma_d R_u T}\right)} - 1\right)\right). \tag{4a}$$

$$g_{ph} = q_e \int_{\lambda=0}^{\lambda \leq \lambda_{bg}} \kappa_{p,\lambda}\, C_p\, \Phi_{y,\lambda}\, d\lambda \tag{4b}$$

The first term, g_{ph}, is the volumetric absorption rate of the incident photons by the particles in the suspension; only photons with energies greater than the semiconductor absorption onset (oftentimes the bandgap) are considered to be absorbed. The second term is the volumetric recombination rate in the absence of illumination with an exponential dependence on the voltage, V_{ph}, and influenced by the surface-specific, radiative recombination current density, j_{rr}, the diode quality factor, γ_d, the operating temperature, $T = ¿$ 298.15 K, and the specific surface area of the

19

semiconductor particles, $A_{0p} = \dfrac{6 C_p}{d_p \rho_p}$, where ρ_p is the bulk density of the

semiconductor particle. A nominal particle diameter, d_p , of 100 nm was used based on

a reported powder-to-agglomerate size range of 10–1000 nm [83] for the OER and the

HER semiconductor particles; however, this was rather inconsequential because modeling

results for reaction rates and STH efficiencies were found to be insensitive to the value of

d_p . This insensitivity is a consequence of the model treating the particles as point

locations and the particle size only implicitly enters the analysis as a scale factor for the

specific surface area, A_{0p} , in eqs. (4a) and (6). The reverse saturation current densities

modeled (eq. (4a)) for the semiconductor particles determines the open-circuit potentials,

with smaller values for j_{rr} increasing the open-circuit potential and improving the

reaction rates by decreasing the recombination rates of the charge-carriers produced.

Reverse saturation current densities have not been reported for semiconductors in the

particle form factor. Therefore, baseline values (Table 2) were selected from

experimentally measured open-circuit potentials for $BiVO_4$ electrodes affecting OER. For

$SrTiO_3$:Rh particles, the baseline reverse saturation current density was chosen to be

several orders of magnitude larger than the detailed balance or Shockley–Queisser limit,

while also being small enough to yield desired rates of product formation. For

comparison, based on the material bandgaps the Shockley–Queisser limits, for TiO_2,

$BiVO_4$, and $SrTiO_3$:Rh are on the order of 10^{-45}, 10^{-35} and

10^{-35} A m^{-2}, respectively at 298.15 K. Furthermore, the sensitivity of model results to the

choice of j_{rr} for the OER and the HER particles was evaluated and the results are

shown in Figure S7. These results indicate that reaction rates expected for reverse

20

saturation current densities dictated by the Shockley–Queisser limit are predicted to be nearly equal to the baseline reaction rates (although the photovoltages are drastically different), suggesting that increasing the sunlight-driven power production of the semiconductor particles, by further decreasing the reverse saturation current densities toward the Shockley–Queisser limits, will not substantially alter the rate of H_2 evolution.

Interfacial Reaction Kinetics

On the surface of the semiconductor particles at least one pair of redox half-reactions occurs. One of the factors that influences the reaction rate is the photovoltage (V_{ph}¿, which is equal to the sum of the surface overpotentials for the two redox reactions and the species-concentration-dependent thermodynamic equilibrium potential (Nernstian potential), U, for the net reaction on the semiconductor particle surface (L1 or L2)

$$V_{ph} = U_{L1/L2} + \left| \eta_{OER/HER} \right| + \left| \eta_{R_c/R_{ox}} \right| \tag{5}$$

The baseline case assumed complete selectivity toward the desired reactions, i.e. L1 and L2 (Figure 1(b)). The flux of electrons/holes across the cocatalyst surface area for the kth reaction (k = OER, HER, R_{rd}, and R_{ox}) is

$$R_{sel,k} = \frac{r_{e/h}}{f_{cat,k} A_{0p}}, \tag{6}$$

where, $f_{cat,k}$ is the fractional coverage of the cocatalyst on the semiconductor particles. In the absence of published data for redox-shuttle-specific reaction rate mechanisms and constants, the interfacial electron transfer rates were obtained by applying simplistic Butler–Volmer kinetic formulations [90] ,

$$R_{sel,k} = \frac{j_{0,k}}{F} \left(e^{\frac{\alpha_{a,k} \eta_k F}{R_u T}} - e^{\frac{-\alpha_{c,k} \eta_k F}{R_u T}} \right), \tag{7}$$

where, $j_{0,k}$ is the exchange current density, $\alpha_{a,k}$ and $\alpha_{c,k}$ are the anodic and cathodic charge transfer coefficients, and η_k is the surface overpotential. Typically, $j_{0,k}$ depends on the electrolyte composition, cocatalyst material, and temperature. For the OER and the HER, the exchange current densities and charge transfer coefficients are based on best-fit parameters obtained from literature data for RuO_2 and Pt, respectively (Table 2). By simultaneously solving equations (4a) through (7), the variables $r_{e/h}, R_{sel,k}, V_{ph}, \eta_{OER/HER}$ and η_{R_{ox}/R_i} can be evaluated. Based on the assumption of $\eta_{R_i} \ll \eta_{OER}$ and $\eta_{R_{ox}} \ll \eta_{HER}$ for the facile redox shuttles, the reduction/oxidation overpotentials for the redox shuttle were neglected in eqs.(5) and (7) in the baseline case that assumed complete reaction selectivity.

Selective catalysis is crucial to achieve large STH efficiencies in particle-suspension reactors, however, in reality each particle is wetted by electrolyte that contains at least four chemical species that can partake in redox chemistry at the particle surface, and a quanta of separated charge could be lost due to recombination to undesired "back-reactions" with two of the species. Note that only particle-mediated surface reactions were considered in this analysis for non-baseline cases, and the homogeneous chemical reactions of the species in the electrolyte were neglected. For example, on the surface of the HER particles the undesired reactions are the dissolved H_2 oxidation reaction (HOR) by holes in the valence band and/or reduction of the oxidized form of the redox shuttle, $D^+ \square D$ (R_{red}), by electrons in the conduction band. These reactions occur simultaneously with the desired surface reactions of HER by electrons in the conduction band and oxidation of the reduced form of the redox shuttle, $D \square D^+$ (R_{ox}), by holes in

the valence band. The overpotentials for these competing reactions on the HER semiconductor particles can be related to the photovoltage in eq. (5) as,

$$\left|\eta_{R_{c/HOR}}\right| = V_{ph} - \left|\eta_{R_{ox/HER}}\right| \tag{8}$$

Butler–Volmer kinetics, as shown in eq. (7), was applied to obtain the rate of competing back-reactions as a function of the respective overpotentials in eq. (8). The effective reaction rate, R_{eff} , was expressed as the difference of the rate of selective catalysis, R_{sel} , and the competitive back reactions, R_{back} . When the back-reaction rates were predicted to be larger than the rates of the desired reactions, particle shunting occurs with unity yield, and the effective reaction rate is zero.

$$R_{eff,j} = R_{sel,j} - R_{back,i} \tag{9}$$

For the OER particles j = OER/R_{red}, i = R_{ox}, ORR and likewise, for the HER particles, j = HER, R_{ox}; i = HOR, R_{red}

Species Transport

For dilute solutions, the Nernst–Planck equation [77] dictates the migration and diffusion species fluxes (convective fluxes are not considered here as a worse-case stationary system is assumed),

$$N_i = -z_i u_i F c_i \nabla \phi - D_i \nabla c_i \tag{10}$$

where, z_i is the charge magnitude, the mobility, u_i , and diffusion coefficient, D_i , for each species are related through the Nernst–Einstein relationship [79], ϕ is the electrolyte potential and c_i is the species concentration of the ith species. The Nernst-Planck equation was assumed operative in the reactor compartments, as well as in the porous separator where an effective diffusivity ($D_{i,eff} = \dfrac{w_{sep} \varepsilon_{sep}}{w_{unit}} D_i$) was used.

Overall mass conservation,

23

$$\frac{\partial c_i}{\partial t} = -\nabla \cdot N_i + r_i \tag{11}$$

and solution electroneutrality,

$$\sum_i z_i c_i = 0 \tag{12}$$

was applied. The source/sink term in eq. (11), r_i, is related to the volumetric rate of charge-carrier production from eq. (4a),

$$r_i = \frac{v_i r_{e/h}}{n} \tag{13}$$

where, v_i is the stoichiometric coefficient for the ith species and n is the number of electrons transferred in the redox reaction considered. In the absence of an external field/current density in the particle-suspension reactor designs,

$$\sum_i N_i z_i = 0 \tag{14}$$

Combining eq. (10) and eq. (14), electrostatic potential gradient in the bulk solution can be related to the diffusion fluxes of ionic species,

$$\nabla \phi = \frac{-\sum_i z_i D_i \nabla c_i}{F \sum_i z_i^2 u_i c_i} \tag{15}$$

Metrics

The projected areal rate of charge-carrier production, R_a, is obtained by spatially integrating the volumetric rate (eq. (13)) in the respective reaction compartment over the two-dimensional reaction compartment surface area, A, and averaging the integrated value over the reaction compartment height,

$$R_a = \frac{\iint r_{e/h} dA}{h} \tag{16}$$

This areal reaction rate is reported here instead of a current density, because, unlike fixed-electrode PEC reactors, particle-suspension designs do not result in a net ionic/electronic current that spans the entire length of the reactor necessitating ion migration and resulting

in ohmic potential drops. From the areal H_2 production rate, the peak and day-averaged STH efficiencies are,

$$\eta_{STH,peak} = \frac{R_{H_2,a}^{max} \Delta G_{O_2/H_2O}^0}{2 I_{AM1.5,max}} \tag{17}$$

$$\eta_{STH,avg} = \frac{\int_{t=m-1}^{t=m} R_{H_2,a} \Delta G_{O_2/H_2O}^0}{2 \int_{t=m-1}^{t=m} I_{AM1.5} dt}, \tag{18}$$

where, m in eq. (18) ranges from 2 to 365 days. At the baseline STH efficiency of 1% and at peak incident solar flux, the areal rate of charge-carrier production is 8.43×10^{-5} mol m^{-2} s^{-1} and the areal H_2 production rate is 4.21×10^{-5} mol m^{-2} s^{-1}.

For the particle-suspension design, potential/energy losses arises due to a change in the concentrations of the reaction species between the two compartments and contributes to spatially variant reaction potentials. This mass-transfer-related potential loss or overpotential, $\Delta \phi_{mt}$, between two locations in the particle-suspension designs ~~with soluble redox shuttles~~, one in the OER compartment and one in the HER compartment, has contributions from pH gradients, $\Delta \phi_{pH}$, and the concentration gradient of the redox shuttle species, $\Delta \phi_{¿}^{D^{+¿/D}}$,

$$\Delta\phi_{mt} = \underbrace{\frac{2.303\,RT\left(pH_{OER}-pH_{HER}\right)}{F}}_{\Delta\phi_{pH}} + \frac{RT}{nF}\ln\frac{\displaystyle HER\,\frac{D^{+¿}}{D}}{\displaystyle \frac{D^{+¿}}{D}} \quad\text{(19)}$$

The species concentrations in eq. (19) are computed as volume-averaged values in the OER and the HER compartments. Ohmic potential losses between the reaction compartments are not present due to the lack of an externally applied field to drive ion transport.

Solution Procedure

The coupled governing equations (eqs. (1), (2), (4a)—(13)) were solved on the two-dimensional numerical domain with the appropriate boundary conditions (Figure 2) using the finite element method on a mapped mesh with a maximum of 10,000 elements. The discretized equations were solved using COMSOL Multiphysics [91] with quadratic element discretization and a time-dependent direct linear solver (PARADISO). Implicit and adaptive time stepping, with a maximum time-step of 600 s, was employed to attain a relative tolerance of 10^{-4} for all the scaled variables. Mesh independence was verified by doubling the mesh size, which yielded a maximum change of 1% in the spatially-averaged species concentrations and the sink-term/source-term computed in eq. (11).

Zero flux boundary conditions were applied for the species concentrations, c_i, and the electrolyte potential, ϕ, at all the domain surfaces as shown in Figure 2. The procedure adopted for the quasi-steady simulations and to determine the initial values of the solution variables for the transient simulations is detailed below. All the simulations were performed on a dual core Intel Xeon X5660 processor (2.8 GHz, 24 GB), and the model developed is robust enough to tackle the various semiconductor particles, redox shuttles and reaction compartment heights investigated in this study. For the largest reaction compartments (10 cm tall) the transient simulations take approximately 8 hours of wall clock time to attain steady-periodic conditions.

Model Simulations

Quasi-steady simulations were performed to evaluate the impacts of the semiconductor and the electrolyte optical properties on the reactor performance in the absence of any mass transport limitations. These simulations used simplified model conditions of peak incident photon flux (i.e. solar noon) and time-invariant and position-invariant concentrations of the electrolyte specie, and essentially only eqs. (4a)– (7) are solved along the height of the reactor. The thermodynamic potentials for effecting reactions L1 and L2 for the various redox species considered are fixed at the respective standard-state values indicated in Table 2. For all these simulations, only the concentrations of the most strongly sunlight-absorbing redox species (i.e. I_3^-, Fe^{3+}, Q and QH_2) were varied. The concentrations of the other redox species (I^-, IO_3^-, and Fe^{2+}), which absorb little light at $\lambda > 280\,nm$, were set to values required to maintain the respective E^0 values (listed in Table 2) because the areal reaction rates were not affected by changes to the concentrations of these redox species. Reaction kinetics is not affected by

27

the concentration of these redox species in the baseline cases that assumed selective surface catalysis where the OER and the HER are rate limiting. For all these cases the proton concentration, $c_{H^{+}}$, was fixed at 1 M. For the Q/QH$_2$ redox shuttle, equal concentrations of Q and QH$_2$ were assumed, and the maximum concentration evaluated was 0.5 M, which is the aqueous solubility of QH$_{2\ [65]}$.

For the transient simulations, species transport, production and consumption (eqs. (8) − (13)) in the reactor are all considered in addition to the spatial profiles of the photon-fluxes and the volumetric reaction rates (eqs. (4a)– (7)) in the presence of diurnal illumination cycles. The spatial and temporal variations of the electrolyte species concentrations and its influence on light absorption, Nernst reaction potential and reaction kinetics are all inherently accounted for in these simulations. For these simulations, at $t=0$ s, the variables $r_{e/h}, R_{sel,k}, \eta_{OER/HER}$ and ϕ were initialized to 0 and the photovoltage, V_{ph} , was set equal to the position-dependent open-circuit potential (from eq. (4a)). The concentrations of electrolyte species required to sustain reactor operation at desired STH efficiencies (D$^+$, D, H$^+$, OH$^-$) were evaluated iteratively from the model results. Guess values for these initial concentrations were obtained by solving the species transport equations, eqs. (10)–(12), with spatially homogeneous reaction rates that were consistent with a 1% STH efficiency at peak solar insolation; the day/night illumination profiles were superimposed on these rates to obtain the transient variations.

RESULTS AND DISCUSSION

The influence of the optical properties of the semiconductor materials and the redox couples on the reactor performance was first evaluated under quasi-steady conditions and in the absence of any mass transport limitations. Transient results that take into consideration effects of species transport and diurnal variations in the incident photon fluxes were then analyzed as well as the impacts of competitive back reactions.

Effects of Optical Properties

Figure 3 shows the impact of competitive light absorption by the redox shuttle for fixed semiconductor particle concentrations of 1 g L^{-1}, with and without tandem light absorption. For both the tandem (Option I) and the same-bandgap cases (Option II), the areal reaction rate decreased exponentially with redox shuttle concentration (Figure 3) due to competitive light absorption. Incorporation of triiodide ions led to the lowest predicted reaction rates in the top and bottom compartments, because I_3^- exhibits the strongest visible light absorption (Figure S1). The rates were slightly larger for Fe^{3+}/Fe^{2+} and even larger for the organic redox couple because these species absorb very little visible
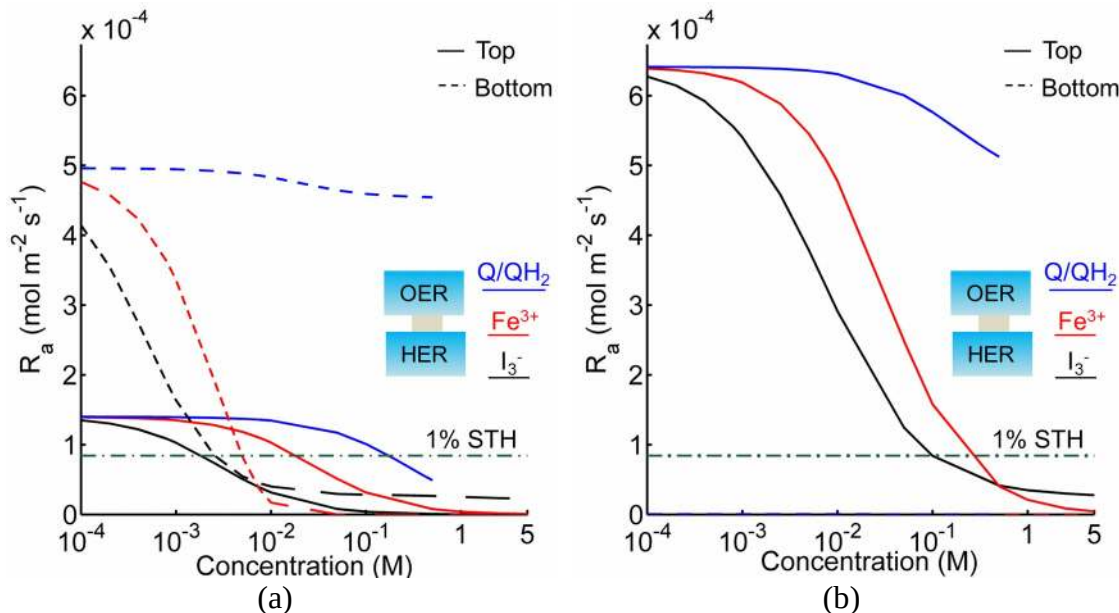
Figure 3. Areal reaction rates as a function of redox shuttle concentration in the top (OER) and bottom (HER) reaction compartments, for 1 cm tall compartments each containing 1 g L^{-1} particles with SrTiO$_3$:Rh in the bottom compartment and the top compartment containing (a) TiO$_2$ (Option I) and (b) BiVO$_4$ (Option II). The areal reaction rate corresponding to the baseline STH efficiency of 1% is 8.43 × 10^{-5} mol m^{-2} s^{-1} and is indicated by the green dashed lines. Bottom compartment rates for Option II are so small that they are not visible in Figure 3(b). I$^-$ and IO$_3^-$ redox shuttle species are not shown here as they do not absorb sunlight in the wavelengths of interest.

light. Option I achieved baseline STH efficiencies in the absence of mass transport limitations when using redox shuttles that contain < 2 mM I$_3^-$ or < 5 mM Fe^{3+}, constraints that arise due to competitive absorption of sunlight. It was determined that, for all redox shuttles considered (Figure 3), the rates in the top OER compartment are larger for Option II (Figure 3(b)) relative to Option I (Figure 3(a)). This effect is because BiVO$_4$ absorbs more sunlight than the wide-bandgap TiO$_2$. However, this improvement in light absorption comes at the expense of the reaction rates in the bottom compartment, which are larger for Option I than Option II owing to improved visible-light transmission to the bottom HER compartment when TiO$_2$ is used in place of BiVO$_4$. The consequence is that the reaction rates for Option II in the bottom compartment are negligibly low even for the

smallest redox shuttle concentration (10^{-4} M) considered (Figure 3(b)). This result suggests that the $BiVO_4$ particle concentration and/or pathlength for light absorption have to be further optimized to achieve the baseline STH efficiency of 1% for Option II.

In addition to the type and redox shuttle concentrations, the reaction rates are influenced by the optical thicknesses of the semiconductor particles (eq. (3a)). Optical thickness linearly depends on the particle concentration (C_p, absorption cross-section ($\acute{\kappa}_p$, and reaction compartment height (h). Figure 4 illustrates the effects of optical thicknesses on the reaction rates in the top and bottom reaction compartments at various concentrations of Q/QH_2 with and without tandem light absorption. The rates in the top compartment are only dependent on the optical thickness of the top compartment, $\tau_{p,top}$ (Figures 4(a), (b)), whereas the rates in the bottom compartment are dependent on the optical thicknesses in both the top and bottom compartments (Figures 4(c), (d)). In both options considered, the reaction rate in the top OER compartment increased asymptotically with optical thickness until a rate of 1.4×10^{-4} mol m^{-2} s^{-1} for Option I (Figure 4(a)), and 6.4×10^{-4} mol m^{-2} s^{-1} for Option II (Figure 4(b)), values that are dictated primarily by the band gap and spectral absorptivities of the particles. Supported by the data in Figure 3, reaction rates decrease as the concentrations of the redox shuttle increase due to competitive light absorption. The reaction rates in the bottom reaction compartment are shown in Figures 4(c), (d) for the largest redox shuttle concentration considered, 0.5 M. Results for the other concentrations of Q/QH_2 show qualitatively similar trends and are presented in Figure S3. In both options, the reaction rates increased as the optical thickness of the $SrTiO_3$:Rh particles, $\tau_{p,bot}$, increased, to a maximum value
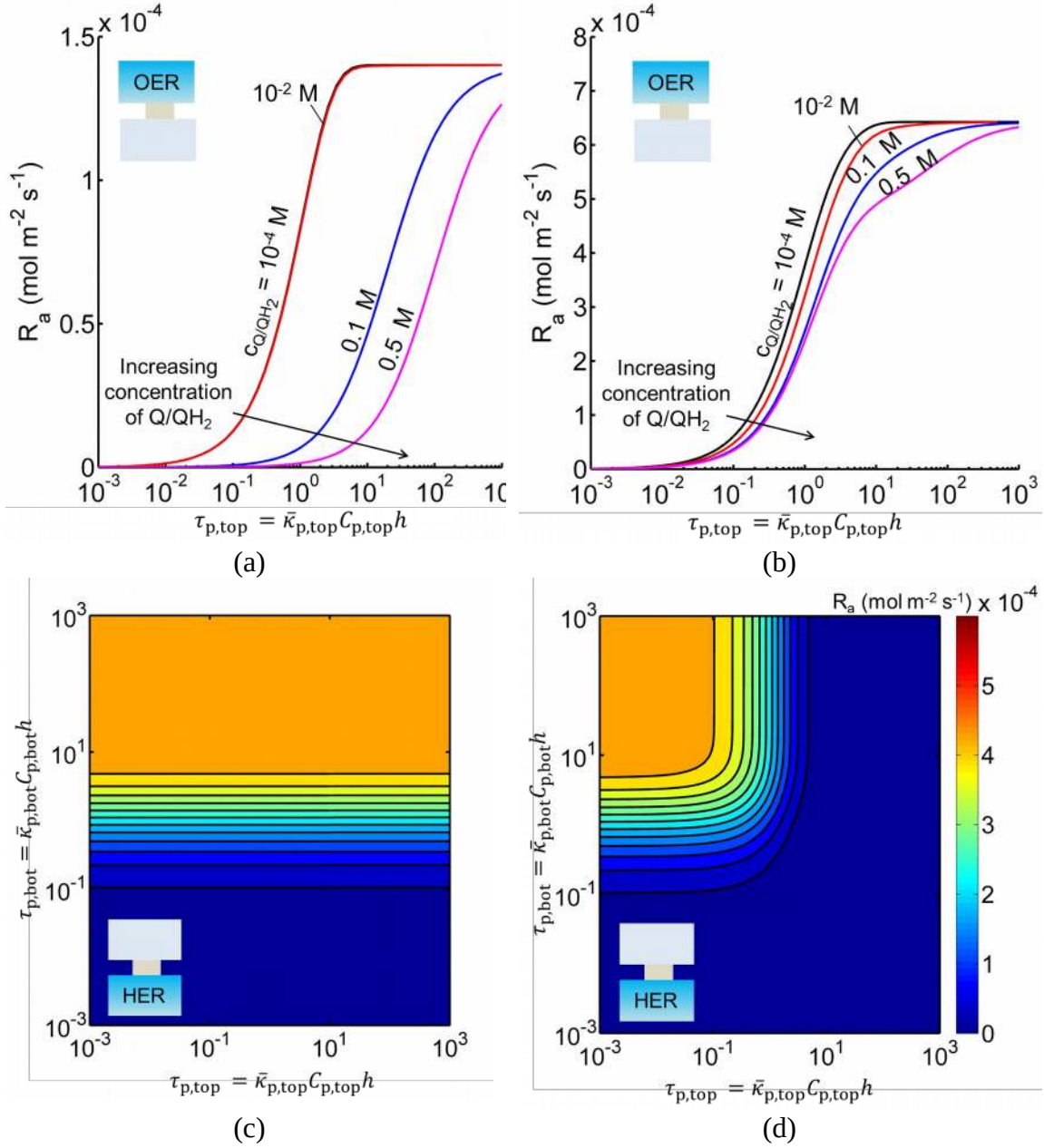
Figure 4. Areal reaction rates in the (a,b) top (OER) compartment as a function of quinone redox shuttle concentration and OER particle optical thickness and in the (c,d) bottom (HER) compartment as a function of OER and HER particle optical thicknesses for (a, c) Option I (TiO_2 (OER) and $SrTiO_3$:Rh (HER)) (b, d) Option II ($BiVO_4$ (OER) and $SrTiO_3$:Rh (HER)) assuming a fixed concentration of 0.5 M for the Q/QH_2 redox shuttle. Particle optical thicknesses linearly depend on the particle concentration, absorption cross-section, and reaction compartment height.

of about 4.5×10^{-4} mol m^{-2} s^{-1}. For Option I (Figure 4(c)), the rates were largely insensitive to the TiO$_2$ particle optical thickness owing to its transmission of light beyond 400 nm, which can be absorbed by SrTiO$_3$:Rh. For Option II, where the particles have similar absorption onsets, a "pseudo-tandem" effect is obtained by modulating the relative optical thicknesses of the top and bottom compartments. If the optical thickness of the top compartment particles is small, $\tau_{top,p} <\, i\,$ 0.01, reaction rates in the bottom compartment were as large as those obtained for the true tandem condition with Option I. These results clearly indicate that the semiconductor particle optical thicknesses have to be optimized to maximize the reaction rates for the OER and the HER in the two compartments. The optimal values are strongly influenced by not only choice of the semiconductor particles in the two reaction compartments, but also the type and concentration of the redox shuttle species considered.

Sustained reactor operation requires equal rates of production and consumption of the redox shuttle species in the two reaction compartments. In Option I, the maximum attainable STH efficiency with sustained operation is limited to ~1.7% because the maximum reaction rate for TiO$_2$ is three times slower than SrTiO$_3$:Rh,
1.4×10^{-4} mol m^{-2} s^{-1} *versus* 4.5×10^{-4} mol m^{-2} s^{-1} (Figures 4(a),(b)). Table 3 presents, for each option for the OER particles and each redox shuttle, the particle optical thickness combinations required to attain the specified STH efficiency with sustained reactor operation assuming rapid mixing that affords fixed redox shuttle concentrations at all spatial locations in the reactor. These results reinforce the negative impacts of competitive light absorption, necessitating rather low concentrations of the I$_3^-$/I$^-$ and Fe^{3+}/Fe^{2+} redox shuttles (< 5 mM) to possibly attain the baseline STH efficiency of 1%.

33

Table 3. Optical thickness combinations for sustained reactor operation at specified values of STH efficiency (%) and redox-shuttle concentrations for Option I (TiO$_2$ (top, OER) and SrTiO$_3$:Rh (bot, HER)) and Option II (BiVO$_4$ (top, OER) and SrTiO$_3$:Rh (bottom, HER)); $j_{rr,OER}=10^{-18}$ A m^{-2}, $j_{rr,HER}=10^{-15}$ A m^{-2} unless otherwise specified; N/A indicates that no optical thickness will yield the indicated STH efficiency (%).

Redox shuttle: I/I$_3$$^-$; $U_{L1}=-0.694$ V and $U_{L2}=-0.536 V$ vs. *NHE*

A/A^- c_i (M)	Option I $\eta_{STH,peak}=¿$ 1%		Option II $\eta_{STH,peak}=¿$ 1%		Option II $\eta_{STH,peak}=¿$ 2%	
	$\tau_{p,top}$	$\tau_{p,bot}$	$\tau_{p,top}$	$\tau_{p,bot}$	$\tau_{p,top}$	$\tau_{p,bot}$
10^{-4}	3.162	0.316	0.178	0.316	0.562	1.778
10^{-3}	31.62	1.77	0.562	3.16	1	N/A
0.1	N/A	N/A	17.78	N/A	56.23	N/A
1	N/A	N/A	177.82	N/A	562.3	N/A

Redox shuttle: Fe^{2+}/Fe^{3+}; $U_{L1}=-0.459$ V and $U_{L2}=-0.771 V$ vs. *NHE*

A/A^- c_i (M)	Option I $\eta_{STH,peak}=¿$ 1%		Option II $\eta_{STH,peak}=¿$ 1%		Option II $\eta_{STH,peak}=¿$ 2%	
	$\tau_{p,top}$	$\tau_{p,bot}$	$\tau_{p,top}$	$\tau_{p,bot}$	$\tau_{p,top}$	$\tau_{p,bot}$
10^{-4}	1	0.316	0.178	0.178	0.316	0.562
10^{-3}	3.162	1.77	0.178	0.562	0.562	1.778
0.1	316.2	N/A	17.78	N/A	56.23	N/A
1	N/A	N/A	177.82	N/A	562.3	N/A

Redox shuttle: Q/QH$_2$; $U_{L1}=-0.53$ V and $U_{L2}=-0.7 V$ vs. *NHE*

A/A^- c_i (M)	Option I $\eta_{STH,peak}=¿$ 1%		Option II $\eta_{STH,peak}=¿$ 1%		Option II $\eta_{STH,peak}=¿$ 3%		Option II $\eta_{STH,peak}=¿$ 3.8%	
	$\tau_{p,top}$	$\tau_{p,bot}$	$\tau_{p,top}$	$\tau_{p,bot}$	$\tau_{p,top}$	$\tau_{p,bot}$	$\tau_{p,top}$	$\tau_{p,bot}$
10^{-4}	0.83	0.186	0.128	0.155	0.47	1	0.77	6.46
10^{-3}	1	0.186	0.155	0.155	0.57	1.2	0.82	9.4
0.1	28.8	0.225	0.27	0.326	1	5.36	1.75	N/A
0.5	128.27	0.225	0.27	0.393	1	5.36	2.1	N/A

Redox shuttle: I$^-$/IO$_3$$^-$; $U_{L1}=-0.145$ V and $U_{L2}=-1.085 V$ vs. *NHE*

$j_{rr,OER}=10^{-18}$ A m^{-2}, $j_{rr,HER}=10^{-20}$ A m^{-2}

Option I $\eta_{STH,peak}=¿$ 1%		Option II $\eta_{STH,peak}=¿$ 1%		Option II $\eta_{STH,peak}=¿$ 3%		Option II $\eta_{STH,peak}=¿$ 3.8%	
$\tau_{p,top}$	$\tau_{p,bot}$	$\tau_{p,top}$	$\tau_{p,bot}$	$\tau_{p,top}$	$\tau_{p,bot}$	$\tau_{p,top}$	$\tau_{p,bot}$
0.91	0.215	0.142	0.17	0.55	1.53	0.72	7.1

These concentrations are prohibitively low, because as discussed next, when mass transport is included in the model, the rate of diffusive species transport is unable to keep up with the rates of redox species consumption/production consistent with a 1% STH efficiency, leading to local depletion of the reactants. For Option II and the quinone redox shuttle, STH efficiencies up to 3% are feasible even with 0.5 M of Q/QH_2, the solubility limit. For lower concentrations of Q/QH_2 ($< 10^{-3}$ M), the largest attainable STH efficiency is 3.8% for sustained reactor operation. For the I^-/IO_3^- redox shuttle, which also undergoes proton-coupled electron transfer, the STH efficiencies are not affected by the redox shuttle concentrations because of their negligible sunlight absorption. However, compared to Q/QH_2, a higher photovoltage (>1.085 V) is required in the HER light absorbers due to the more positive standard-state potential of the I^-/IO_3^- redox shuttle. This large photovoltage requirement can only be obtained when a smaller reverse saturation current density, j_{rr}, of 10^{-20} A m^{-2} is utilized for the SrTiO$_3$: Rh particles in place of the t̶a̶b̶u̶l̶a̶t̶e̶d̶ baseline value of 10^{-15} A m^{-2}. In that case, the maximum attainable STH efficiency for the I^-/IO_3^- redox shuttle is 3.8%, the same maximum value obtained for the Q/QH_2 redox shuttle.

Effect of Species Transport

Based on the model predictions that indicate that Option II has larger theoretically achievable efficiencies (Table 3), this option was chosen for further investigation to evaluate the effects of coupled light absorption, species transport, and reaction kinetics. Transient reactor performance is shown in Figure 5 for the Q/QH_2 redox shuttle, which is projected to attain larger than baseline STH efficiencies for all redox species concentrations considered. The locations of the redox chemistries are opposite of that
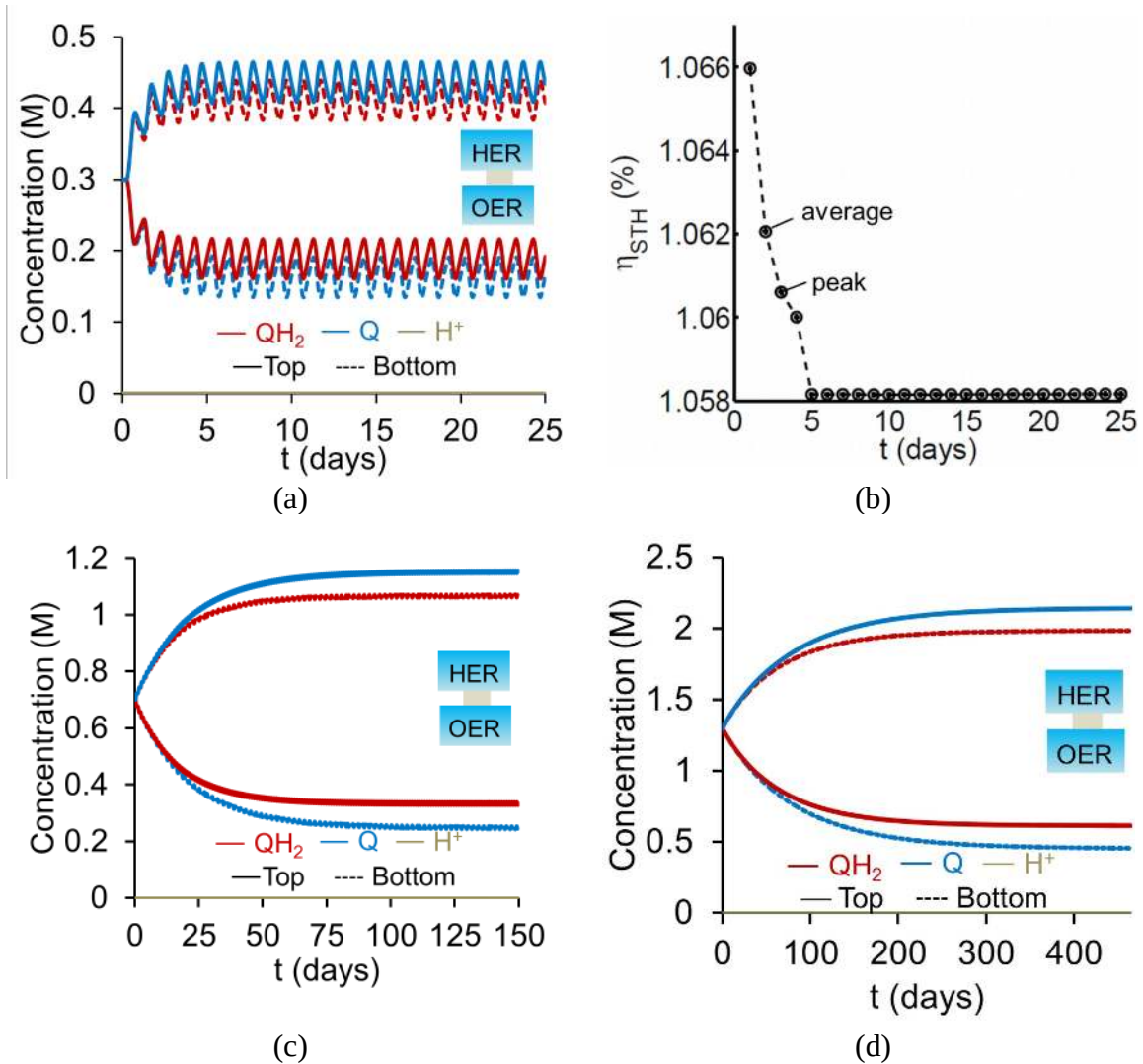
Figure 5 Transient concentration profiles, ((a), (c), (d)) with Option II for reactor heights and SrTiO$_3$:Rh (top, HER), BiVO$_4$ (bottom, OER) concentrations of (a,b) 1 cm and 1.53×10^{-3} g L^{-1}, 2.12×10^{-3} g L^{-1}, and (b) average and peak values for STH efficiency and dashed lines are provided to guide the eye, (c) 5 cm and 0.32×10^{-3} g L^{-1}, 0.43×10^{-3} g L^{-1}, and (d) 10 cm and 0.16×10^{-3} g L^{-1}and 0.2×10^{-3} g L^{-1}.

shown in Figure 1, with HER/R$_{ox}$ in the top compartment and OER/R$_{red}$ in the bottom compartment. The optical properties of Q/QH$_2$ are less detrimental in this modified configuration, suggesting that this arrangement could be more efficient with this redox shuttle. The data indicate that a steady-periodic state of reactor operation is attained after about 5 days, 125 days, and 500 days for 1 cm, 5 cm, and 10 cm tall reaction

compartments, respectively. Figure 5(b) illustrates that the peak and day-averaged STH efficiencies are ~1.06%, which remains constant beyond five days of reactor operation. Stable steady-periodic operation is also observed for the 5 cm and 10 cm tall compartments, as shown in Figures 5(b) and (c), and for operation at the same baseline STH efficiency of ~1%. For each of these conditions, the areal reaction rates (not shown) in the two compartments are very similar during steady-periodic reactor operation. The time taken to attain steady-periodic conditions is computed as the time after which the percentage changes in species concentrations (spatially-averaged concentrations in each reaction compartment) are less than 0.1% from the concentrations predicted in the previous illumination cycle and when the STH efficiency remains constant (as shown in Figure 5(b)). In comparison, an order-of-magnitude estimate for the diffusion timescales, $t_{diff} \sim h^2/D_i$, are 2 days, 50 days and 250 days for respective reaction compartment heights of 1 cm, 5 cm and 10 cm, and computed using the diffusivity of *para*-benzoquinone (slowest diffusing species in the suspension). Model predictions align with the expectation that steady-state conditions will prevail for timescales larger than the diffusion timescales, and in this case, $t_{steady} \sim 2.5\, t_{diff}$. The fact that the predicted time to attain the steady-periodic state is approximately proportional to the square of the compartment height $\left(t_{steady} \propto h^2\right)$, is indicative of a diffusion controlled process. Without day-and-night variations in the incident sunlight, local depletion of the redox species (Q) occurs within a day of reactor operation for the 1 cm tall reaction compartments (Figure S4). Therefore, much larger initial redox species concentrations (0.65 M *versus* 0.3 M for $h = ¿$ 1 cm) are required to attain steady-state conditions for this situation. Irrespective of the pH, the concentration of protons is time-invariant and position-

invariant because it was assumed that the Q/QH$_2$ redox shuttle underwent proton-coupled electron transfer with unity yield in these simulations. Therefore, any pH (pH = 7 in Figure 5) is sustainable using this reactor design, provided that the redox shuttle undergoes rapid proton-coupled electron transfer. At a fixed STH efficiency, the volumetric reaction rate varies inversely with the reaction compartment height, whereas the rate of diffusive species transport decreases proportional to the square of the height. Therefore, to maintain steady and sustained reactor operation, at roughly 1% STH efficiency, the minimum initial concentrations of the redox shuttle increases nearly

linearly with the reaction compartment height $c_{steady} \propto h$). Slight deviations from linearity occur due to the spatial location and concentration dependence of the reaction rates, and the minor differences in the STH efficiencies obtained with the different heights of the reaction compartments. Overall, these scaling relationships underscore the dominance of diffusion as a mode of species transport in the solution compared to migration. For the neutral Q/QH$_2$ redox shuttle, results in Figure 5 demonstrate species mixing entirely controlled by diffusion (in the absence of any forced/natural convection). This result is because with spatially invariant proton concentrations, the net diffusive flux of *any charged species is zero*, i.e. the numerator in eq. Error: Reference source not found is zero. In the absence of an externally applied field or current density, the driving force for ion migration is essentially zero.

For all the reaction compartment heights considered, the potential losses associated with pH gradients are zero with the quinone redox shuttles because the proton concentrations in the solution are spatio-temporally invariant. The mass-transfer overpotential due to the redox species concentration gradients attains a maximum of

28 mV, 33 mV, and 35 mV during steady-periodic reactor operation for the 1 cm, 5 cm, and 10 cm tall reactors.

For reaction compartment heights greater than 5 cm the predicted concentration profiles in Figure 5 suggest that sustained reactor operation, is limited by the aqueous solubility of Q and QH_2. Even for $h = ¿$ 1 cm, the required concentration of Q for sustained reactor operation is larger than its aqueous solubility limit of 0.1 M. While aqueous solubility can be improved through introduction of sulfonate groups on the redox shuttle molecules [65], these large groups also reduce species diffusivities and therefore, optimization of these tradeoffs is required. Therefore, one solution to enable sustained reactor operation via diffusive species transport with reasonable concentrations of these redox shuttles, is to reduce the reaction compartment heights to the sub-centimeter length scales with concomitant increase in the semiconductor particle concentration to maintain the same reaction rates.

Profiles along the reactor height are informative when visualizing the conditions present under steady-periodic operation. Therefore, depicted in Figure 6 are the following parameter profiles at solar noon for h = 1 cm: redox shuttle concentrations, volumetric reaction rates, photovoltages, and reaction overpotentials. The concentration profiles (Figure 6(a)) are reflected about the center of the reactor ($x = 0, y = 0 ¿$ with equal rates of production and consumption of the redox shuttle in the two compartments during steady-periodic operation. The spatial profiles of the volumetric reaction rates, photovoltage, and overpotentials (Figure 6(b) – (d)) follow the trend of the absorbed
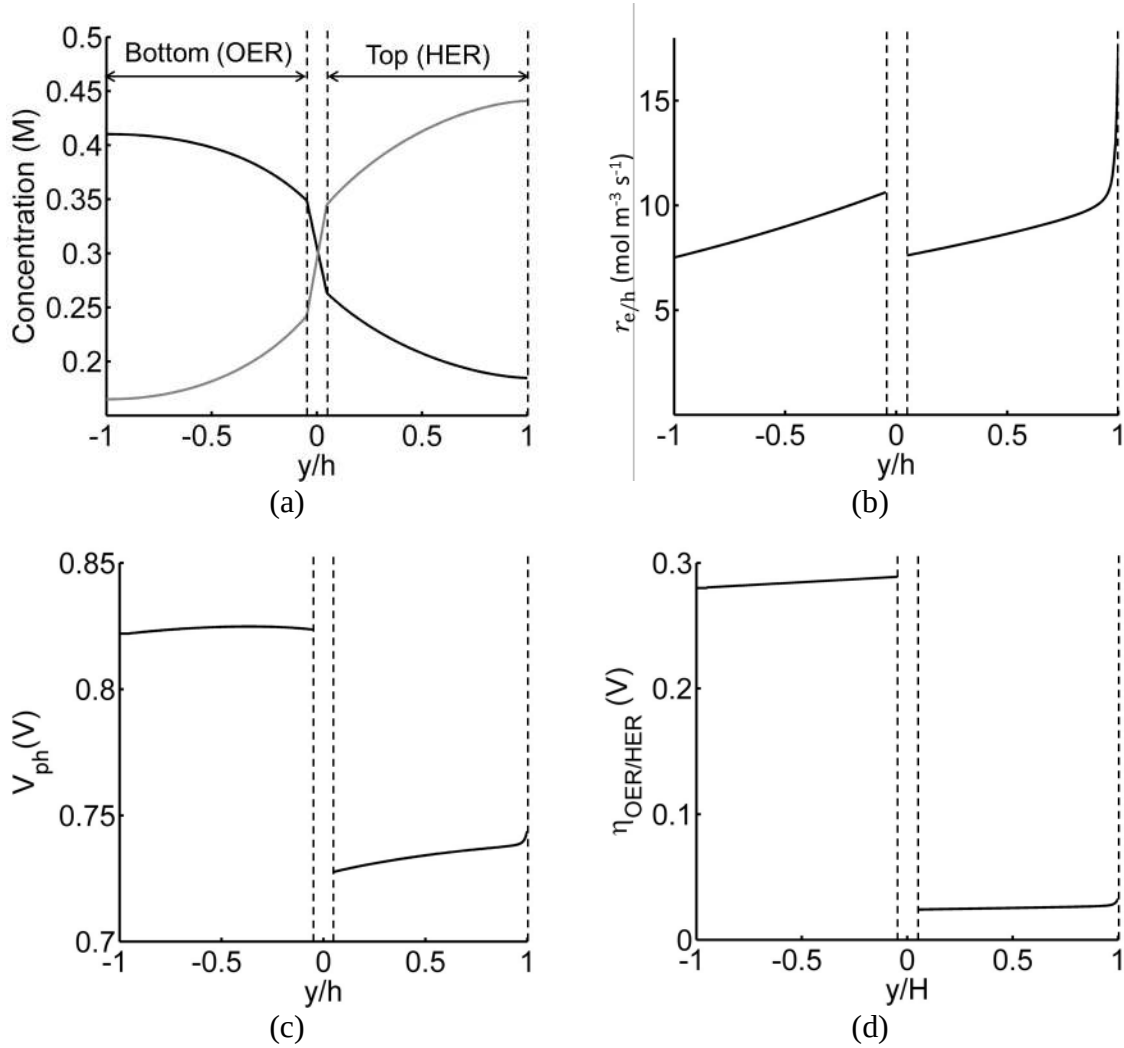
39

Figure 6. Spatial profiles along the reactor centerline at $x = 0$ (see Figure 2) during steady-periodic operation at solar noon with 1.53×10^{-3} g L^{-1} of SrTiO$_3$:Rh in the top (HER) reaction compartment and 2.12×10^{-3} g L^{-1} of BiVO$_4$ in the bottom (OER) reaction compartment: (a) redox shuttle concentrations, (b) volumetric rates of charge-carrier production, $r_{e/h}$, (c) photovoltage, V_{ph}, and (d) reaction overpotentials, $\eta_{OER/HER}$.

photon flux and therefore, decrease along the reactor height. The relatively more linear spatial profiles of the volumetric reaction rate in the bottom compartment in comparison to the top compartment are due to the differences in the optical properties of the semiconductor materials and the increased light attenuation by the electrolyte along the reactor height. The average photovoltage produced by the photocatalysts that drive R$_{ox}$/HER is 0.734 V, while the photovoltage is ~100 mV larger at 0.824 V for the

photocatalyst particles that implement OER/R_{red}, which is in part required to supply the larger overpotentials for the OER (Figure 6(d)).

In addition to the Q/QH$_2$ redox shuttle, transient reactor performance was also evaluated for the IO$_3^-$/I$^-$ redox shuttle (Figure S5), which is also predicted to achieve baseline and up to 3.8% STH efficiency like the quinone redox shuttles (Table 3). With exceptions of the requirements of larger photovoltages from the HER semiconductor particles than with the Q/QH$_2$ redox shuttle and the need for more alkaline conditions to favor conversion of I$^-$ to IO$_3^-$ instead of strongly-visible-light-absorbing I$_3^-$, the results using this redox shuttle are promising. Sustained reactor operation at a 1% STH efficiency is achieved with redox shuttle concentrations well below their solubility limits even for 10 cm tall reactor compartments (see Figure S5), and Figure S6 shows that diffusion-driven species transport is able to sustain reactor operation at 3.8% STH efficiency with 1 cm tall reaction compartments for the IO$_3^-$/I$^-$ redox shuttle. The mass-transfer overpotential due to the redox species concentration gradients has a maximum of 11 mV for the 10 cm tall reaction compartments during steady-periodic operation.

For the strongly-visible-light-absorbing I$_3^-$/I$^-$ and Fe^{3+}/Fe^{2+} redox shuttles, because concentrations less than 5 mM are required to minimize the impacts of competitive light absorption, diffusion distances less than 0.01 cm are needed to sustain the reaction rates corresponding to the baseline STH efficiency of 1%. However, this short distance implies that impractically large semiconductor particle concentrations, i.e. > 10 g L^{-1}, are required to achieve the required optical thicknesses reported in Table 3. Moreover, reactor heights on the sub-mm lengthscale will be extremely challenging to fabricate and to prevent bubble occlusion. For taller reaction compartments, $h > ¿$ 0.01 cm, the diffusion-

41

sustained STH efficiencies are restricted to less than 0.2% due to competitive light absorption by I_3^- and Fe^{3+} redox species, as suggested by Figure S4. Because these redox shuttles are not modeled to undergo proton-coupled electron transfer, spatial gradients in pH and the redox shuttle species concentration gradients result in mass-transfer-related overpotentials. However, at low STH efficiencies of 0.2%, these overpotentials are less than 1 mV. These results indicate that reactor heights on the lengthscales of centimeters are best to achieve the 1% baseline STH efficiency for the I_3^-/I^- and Fe^{3+}/Fe^{2+}, provided that some form of active species mixing is possible.

Effects of Competitive Surface Reactions

The above analysis assumed perfectly selective reactions without considering the overpotentials for the undesired back reactions. Figure 7 shows the impacts of the redox shuttle kinetic parameters for Q/QH_2 on the competing back reactions of redox chemistry with the redox shuttle species. The effective reaction rates (R_{eff} , eq. (9)) are normalized with the baseline rates obtained in Figure 6, which assumed selective surface catalysis. The overpotential for oxidation of liberated H_2 by holes in the valence band for the HER particles is large (> 1.23 V), and the models predict very rapid hydrogen oxidation, so much so that in the absence of active removal of H_2 or asymmetric charge transfer coefficients for the HER there is no net desired H_2 formation (data not shown). For all exchange current densities investigated for the redox shuttle, symmetric charge-transfer
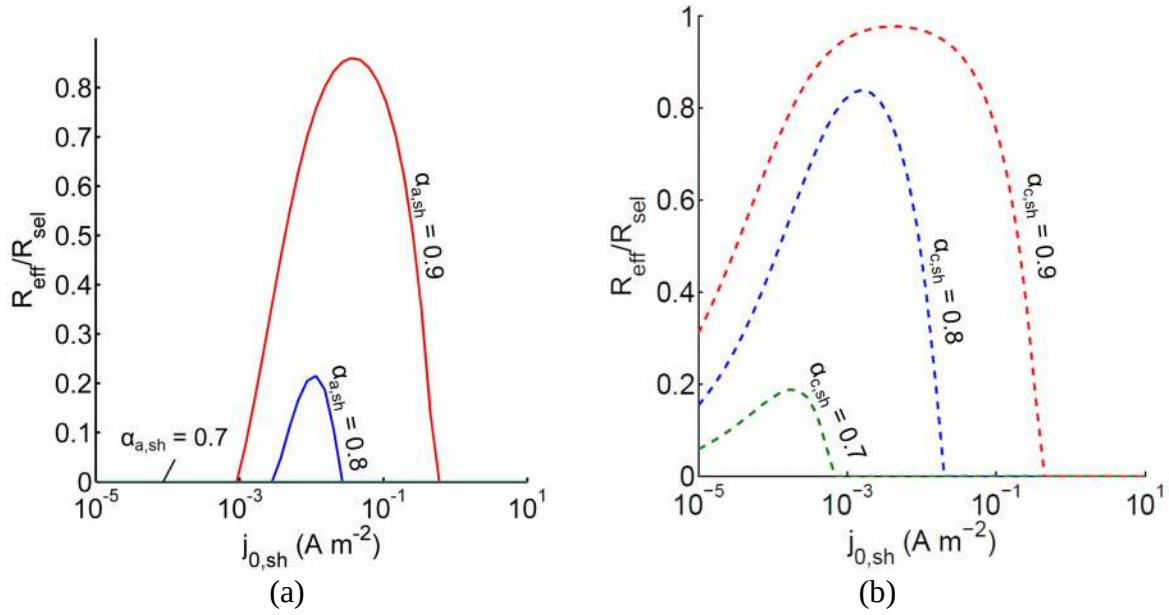
Figure 7. Effective redox shuttle reaction rates, R_{eff} , normalized to the baseline reaction rate, $R_{sel,k}$, that assumed selective catalysis as a function of kinetic parameters ($j_{0,sh}$, $\alpha_{a,sh}$ and $\alpha_{c,sh}=1-\alpha_{a,sh}$) for $h=1$ cm with the Q/QH$_2$ redox shuttle at concentration ratios that are consistent with the steady-periodic results from Figure 5 (i.e. $\frac{c_Q}{c_{QH_2}}$ *H tent with the prrier reaction rates ofon rates compared ¿ the base − case results rates for the light cathodi* equals 2.56 and 0.44 in the HER (top) and the OER (bottom) compartments, respectively) for (a) SrTiO$_3$:Rh (top, HER) and (b) BiVO$_4$ (bottom, OER) particles.

coefficients ($\alpha_{a,sh}=\alpha_{c,sh}=0.5$ ¿ resulted in net rates that were zero. Figure 7(a) suggests that for asymmetric charge-transfer coefficients there is an optimum redox shuttle exchange current density to maximize the resultant surface reaction rate in the presence of back reactions of the redox shuttle, in this case, the reduction of Q. The contending effects are that an increase in the exchange current density reduces the overpotential for the oxidation (QH$_2$ to Q) and thereby, intensifies the driving force for the reduction reaction, which acts as a recombination pathway shunt. For smaller exchange current densities, the overpotential increases for the oxidation reaction, and shifts the photovoltage closer to the open-circuit potential of the photodiode, which

diminishes the reaction rate. With increase in the anodic charge transfer coefficient, $\alpha_{a,sh}$, the oxidation of QH_2 is favored more than the reduction of Q, and therefore the resultant reaction rates increase. The highest predicted rate for the case of $\alpha_{a,sh}=0.9$ with the selected concentration ratio is at least 15% smaller than the baseline reaction rate without competing surface reactions.

Oxygen reduction suing the OER particles is much more challenging than H_2 oxidation using the HER particles owing to the relatively low cathodic transfer coefficient to effect the oxygen reduction reaction ($\alpha_{c,OER}=0.1$ compared to $\alpha_{a,OER}=1$ [27,67,68]). The resultant reaction rates change by less than 3% when back reactions with dissolved O_2 are taken into account, and therefore, those results are indistinguishable from the results shown in Figure 7(b). Similar to the HER particles, symmetric charge transfer coefficients result in no net desired reactions and an optimum exchange current density arises due to the tradeoffs in decreasing the overpotential of the desired reaction ($R_{\dot{c}}$ in this case) for larger values of $j_{0,sh}$ and operating near the open-circuit potential of the modeled photodiode when the exchange current density is low. The optimum exchange current densities are in general lower compared to those of the HER particles for all cases considered, and the highest reaction rate for the case of $\alpha_{c,sh}=0.9$ is only 2% lower than the baseline reaction rate. These contrasting effects are due to the relatively larger open-circuit photovoltage modeled for the $BiVO_4$ particles than in the $SrTiO_3$:Rh particles of 1.06 V *versus* 0.88 V, respectively. Figure 7 is suggestive that redox shuttles with asymmetric charge-transfer coefficients and small exchange current densities (typically $< 1 \, A \, m^{-2}$) are likely to result in larger STH efficiencies.

44

Figure 8 shows the variations in the effective redox shuttle reaction rates normalized to the baseline reaction rates as the ratio of the concentrations of the reduced and oxidized forms of the redox shuttle varies from 0.1 to 10. The concentration ratio affects the driving force for the redox shuttle reactions via the Nernst equation such that larger driving forces result in faster reactions. The optimum exchange current density decreases as the concentration ratio is modified such that it favors the desired reactions by reducing the reaction overpotentials (decreased/increased redox shuttle concentration ratio for the HER/OER particles, respectively).
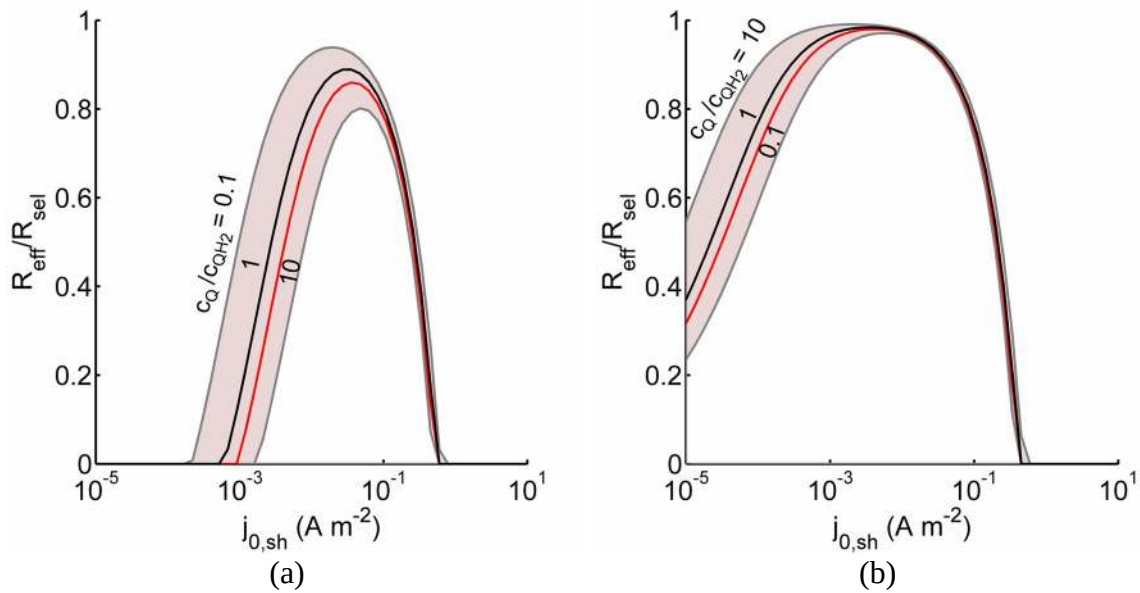

(a)   (b)

Figure 8. Effective redox shuttle reaction rates normalized to the baseline reaction rate, $R_{sel,k}$, that assumed selective catalysis as a function of kinetic parameters ($j_{0,sh}$, $\frac{c_Q}{c_{QH_2}}$ *H tent with the prrier reaction rates of on rates compared ¿ the base − case results rates for the light cathodi*) for $h=1$ cm and the Q/QH$_2$ redox shuttle with (a) SrTiO$_3$:Rh (HER), $\alpha_{a,sh}=0.9$, and (b) BiVO$_4$ (OER), $\alpha_{c,sh}=0.9$ particles. The solid red line corresponds to values of $\frac{c_Q}{c_{QH_2}}$ consistent with steady-periodic results in Figure 5 with (a) $\frac{c_Q}{c_{QH_2}}=\mathrm{¿}$

H tent with the prrier reaction rates of on rates compared $\dot{c}$ the base $-$ case results rates for the light cathodic $\wedge$ p

2.56 and (b) $\dfrac{c_Q}{c_{QH_2}} = \dot{c}$ 0.44.

Comparison with fixed-electrode PEC designs

The most important aspect of the particle-suspension reactor is that local currents between sites of anodic (holes) and cathodic (electrons) reactions are very small, even for efficient designs that generate O_2 and H_2 at a rate consistent with the benchmark current density for an efficient solar water splitting device of 20 mA cm^{-2}. This is because these reaction rates are distributed over the height of the compartment such that on average the rates are consistent with a current density of $20/n$ mA cm^{-2}, for a reactor with n particles in the optical pathlength to attain the benchmark current density. For the particles modeled in this study the current densities were at most 20 µA cm^{-2} particle^{-1}, which results in a reaction rate expressed as an effective volumetric current density of 250 attoA/particle. These calculations assumed 1 cm tall reaction compartments, maximum particle concentration of 5 g L^{-1} and $d_p = \dot{c}$ 100 nm, to attain the benchmark current density. One benefit of the small local currents present in particle-suspension reactors is that it results in negligibly low ohmic potential losses in the solution. For a single semiconductor particle with radius of 100 nm to at most several microns, the ohmic potential drop due to migration of ions between the sites of anodic and cathodic reactions is expected to be negligibly small (< 1 mV), even when using water with little-to-no supporting electrolyte and only redox shuttles [20]. However, ionic migration over the small lengthscales of individual particles makes separation of the anodic and cathodic reactions on their surfaces nearly impossible, meaning that incorporation of a membrane between those sites becomes challenging. Therefore, highly selective particle reactivity,

as shown in Figure 7, is required to achieve large efficiencies. This is in contrast to the fixed-electrode PEC designs where membrane separators are common and the device dimensions, including species transport lengthscales and operating conditions, must be carefully optimized to minimize the ohmic potential drop and the overall solution transport losses, often to a target value of less than 100 mV [28,31].

Another benefit of the small local currents present in efficient particle-suspension reactors is that near-neutral pH conditions can be used, yet, little-to-no variation in the local pH is generated during operation on the surface of an individual particle. Changes in local pH are detrimental to device efficiency because they result in potential losses, as described in eq. (19). This is in stark contrast to the fixed-electrode designs that are incorporated with membranes, where local pH gradients are much more likely to be generated, especially at near-neutral pH conditions. Even for pH 1 electrolytes the pH gradient potential loss is roughly 70 mV for a fixed-electrode PEC device operating at a 10% STH efficiency [31].

Even in the absence of a local pH gradient on the particle surface, there are potential losses due to pH gradients between the OER compartment and the HER compartment in the particle-suspension reactor designs. These losses are anticipated to be similar in magnitude to those observed in fixed-electrode designs. An approximately 60 mV pH gradient loss was evaluated for a hypothetical simulation case operating at 10% STH efficiency and using the I_3^-/I^- redox shuttle. The pH losses are however nearly zero for redox shuttles that undergo rapid proton-coupled electron-transfer. Also, in the particle-suspension reactor designs, additional potential losses occur due to redox shuttle concentration gradients, the magnitude of which depends greatly on the diffusion

lengthscales in the absence of active mixing. Shorter compartment heights facilitate rapid mass transport and decrease this loss, but require a concomitant increase in the concentrations of semiconductor particles to maintain the same performance. These losses are not present in fixed-electrode PEC designs.

A related aspect to the small local currents is that particle-suspension reactors facilitate *volumetric*, three-dimensional reactivity in comparison to the fixed-electrode, wafer-based PEC device designs that drive areal, interfacial activity. In the suspension reactors, the overall reaction rates are distributed throughout the active semiconductor particle surface sites, behavior that is similar to mesoporous electrodes [92,93] and microwire/nanowire array designs [94–96]. This redistribution of the charge carriers and reaction sites reduces the charge-carrier flux to the surface and lowers the reaction overpotentials at any point location. Similar to other micro-structured and nano-structured PEC designs, the high specific-surface areas of the suspended semiconductor particles can enhance the redox-active surface area per unit sunlight collection area compared to the fixed electrode devices and increase efficiency and scalability, assuming that recombination rates are not limited by surface processes. If surface or near-surface sites facilitate recombination, then the benefit of low electrocatalytic rates is at least in part negated by lower observed photovoltages [97]. Finally, particle-suspension reactors can tolerate particle failure (e.g., due to corrosion), because it may not impact other particles to cause a catastrophic failure in the entire device. This is not the case in many fixed-electrode designs where impurities or surface oxides introduce detrimental recombination centers, even at very low concentrations, which then affect the efficacy of

48

charge carriers over a much larger area than just the size (cross-section) of the recombination center.

CONCLUSION

For the first time, the combined effects of device design and choice, and concentrations of semiconductor particles and redox shuttles were numerically evaluated to understand their effects on the overall performance of a vertically stacked, particle-suspension reactor with soluble redox shuttles implementing Z-scheme solar water splitting. The feature that distinguishes the proposed reactor design from prior work is that the compartments effecting the OER and the HER were optically in series, which facilitated tandem light absorption and larger possible STH efficiencies. A transient, two-dimensional reactor model was developed to identify the reaction compartment heights and the operating conditions to achieve sustained reactor operation at 1% STH, facilitated by only diffusion. The volumetric rates of H_2 and O_2 generation in the reaction compartments were evaluated by coupling the photodiode (photo)current—voltage relationship with Butler–Volmer electron transfer kinetics, and taking into account volumetric light absorption and recombination effects in the suspension. The two materials options that were considered for the OER semiconductor particles were TiO_2 and $BiVO_4$, while $SrTiO_3$:Rh was the HER semiconductor particle for all cases. The redox shuttles investigated included I^-/I_3^-, Fe^{2+}/Fe^{3+}, I^-/IO_3^-, and Q/QH_2, with the last two modeled as proton-coupled electron transfer redox reactions.

The optical thickness of the semiconductor particles, which is proportional to particle concentration and absorption cross-section, and reaction compartment height,

49

emerges as an important dimensionless parameter, and was optimized specific to the redox shuttle considered to attain the desired STH efficiency. Results illustrated that amongst the redox shuttles considered, Q/QH_2 and IO_3^-/I^- are more promising than I_3^-/I^- and Fe^{3+}/Fe^{2+} owing to substantial visible light absorption by I_3^- and Fe^{3+} redox species. Competitive light absorption by the I_3^- and Fe^{3+} redox species restricts their concentrations to 5 mM, to attain 1% STH efficiency, requiring small reaction compartment heights and subsequently unrealistically high particle concentrations. OER semiconducting particles consisting of $BiVO_4$ outperformed those consisting of TiO_2, and were projected to achieve STH efficiencies of 3.8% and 1.7% respectively with the Q/QH_2 and IO_3^-/I^- redox shuttles. Species transport is dominated by diffusion over migration for all the reaction compartment heights considered, and purely diffusion driven for the neutral, proton-coupled-electron-transfer quinone redox shuttles. The baseline STH efficiency and steady-periodic reactor operation was attained within the first five days of operation for 1 cm tall reaction compartments with 2.12/1.53 mg L^{-1} of $BiVO_4/SrTiO_3$:Rh particles for the Q/QH_2 redox shuttles. Because of the drawback of a low aqueous solubility for *p*-benzoquinone, the quinone redox shuttle is not anticipated to sustain larger STH efficiencies. On the other hand, the IO_3^-/I^- redox shuttles achieved sustainable baseline STH efficiency while maintaining concentrations below their solubility limits even for 10 cm tall reaction compartments. These model predictions assumed that the HER particles generated photovoltages larger than 1.04 V, which poses both challenges and great opportunities for continued research into these HER semiconducting materials. For both these proton-coupled electron transfer redox shuttles potential losses due to pH gradients are absent, and the species concentration gradients

50

yield a maximum mass-transfer overpotential of 35 mV and 11 mV with the Q/QH_2 and IO_3^-/I^- redox shuttles for 10 cm tall reaction compartments.

In the particle-suspension reactor designs, a fixed areal reaction rate or current density of H_2 generation is divided into much smaller localized anodic and cathodic reaction rates (current densities) as compared to the fixed-electrode counterparts, which results in negligible ohmic/migration potential losses. However, this attribute also poses challenges for placement of membranes between the reaction sites, making selective surface catalysis a crucial requirement for improving the efficiency of these reactor designs. Facile/reversible redox shuttles with symmetric charge transfer coefficients and large exchange current densities lead to large rates for shunting reactions. Asymmetric charge transfer coefficients and optimal exchange current densities for the redox shuttle are required to suppress these undesired back reactions.

In summary, based on model predictions, the proposed reactor design is prospective to sustain at least a 1% STH efficiency with $BiVO_4$ and $SrTiO_3$:Rh photocatalyst particles, aided by diffusive transport of Q/QH_2 and IO_3^-/I^- redox shuttles; the latter redox shuttle exhibits promise of achieving STH efficiencies up to 3.8%. While the model was applied to consider specific photocatalyst materials and redox shuttles, the model formulation is general and can be widely applied for any material and redox shuttle of interest. The effects of particle size and detailed particle-scale photophysics, and natural convection induced species mixing on the overall reactor performance were precluded from this study, but we anticipate that they will be influential parameters to be considered in future work.

REFERENCES

[1]   M. Grätzel, Photoelectrochemical cells, Nature. 414 (2001) 338–344. doi:10.1038/35104607.

[2]   N.S. Lewis, D.G. Nocera, Powering the planet: Chemical challenges in solar energy utilization, Proc. Natl. Acad. Sci. 103 (2006) 15729–15735. doi:10.1073/pnas.0603395103.

[3]   N.S. Lewis, Research opportunities to advance solar energy utilization, Science (80-.). 351 (2016) aad1920-aad1920. doi:10.1126/science.aad1920.

[4]   T.J. Jacobsson, V. Fjällström, M. Edoff, T. Edvinsson, Sustainable solar hydrogen production: from photoelectrochemical cells to PV-electrolyzers and back again, Energy Environ. Sci. 7 (2014) 2056. doi:10.1039/c4ee00754a.

[5]   M. Carmo, D.L. Fritz, J. Mergel, D. Stolten, A comprehensive review on PEM water electrolysis, Int. J. Hydrogen Energy. 38 (2013) 4901–4934. doi:10.1016/j.ijhydene.2013.01.151.

[6]   M. Schreier, L. Curvat, F. Giordano, L. Steier, A. Abate, S.M. Zakeeruddin, et al., Efficient photosynthesis of carbon monoxide from CO2 using perovskite photovoltaics, Nat. Commun. 6 (2015) 7326. doi:10.1038/ncomms8326.

[7]   J.H. Montoya, L.C. Seitz, P. Chakthranont, A. Vojvodic, T.F. Jaramillo, J.K. Nørskov, Materials for solar fuels and chemicals, Nat. Mater. 16 (2016) 70–81. doi:10.1038/nmat4778.

[8]   C. Graves, S.D. Ebbesen, M. Mogensen, K.S. Lackner, Sustainable hydrocarbon fuels by recycling CO_2 and H_2O with renewable or nuclear energy, Renew. Sustain. Energy Rev. 15 (2011) 1–23. doi:10.1016/j.rser.2010.07.014.

[9]   C.L. Muhich, B.D. Ehrhart, I. Al-Shankiti, B.J. Ward, C.B. Musgrave, A.W. Weimer, A review and perspective of efficient hydrogen generation via solar thermal water splitting, Wiley Interdiscip. Rev. Energy Environ. (2015). doi:10.1002/wene.174.

[10]   B.J. Hathaway, R. Bala Chandran, A.C. Gladen, T.R. Chase, J.H. Davidson, Demonstration of a Solar Reactor for Carbon Dioxide Splitting via the Isothermal Ceria Redox Cycle and Practical Implications, Energy & Fuels. 30 (2016) 6654–6661. doi:10.1021/acs.energyfuels.6b01265.

[11]   J.R. Bolton, Solar photoproduction of hydrogen: A review, Sol. Energy. 57 (1996) 37–50. doi:10.1016/0038-092X(96)00032-1.

[12]   J.W. Ager III, M. Shaner, K. Walczak, I.D. Sharp, S. Ardo, Experimental Demonstrations of Spontaneous, Solar-Driven Photoelectrochemical Water Splitting, Energy Environ. Sci. 8 (2015) 2811–2824. doi:10.1039/C5EE00457H.

[13]   R.L. House, N.Y.M. Iha, R.L. Coppo, L. Alibabaei, B.D. Sherman, P. Kang, et al., Artificial photosynthesis: Where are we now? Where can we go?, J. Photochem. Photobiol. C Photochem. Rev. 25 (2015) 32–45. doi:10.1016/j.jphotochemrev.2015.08.002.

[14]   M.A. Modestino, S. Haussener, An Integrated Device View on Photo-Electrochemical Solar-Hydrogen Generation., Annu. Rev. Chem. Biomol. Eng. 6 (2015) 13–34. doi:10.1146/annurev-chembioeng-061114-123357.

[15]   C. Xiang, A.Z. Weber, S. Ardo, A. Berger, Y. Chen, R. Coridan, et al., Modeling, Simulation, and Implementation of Solar-Driven Water-Splitting Devices, Angew.

Chemie Int. Ed. 55 (2016) 12974–12988. doi:10.1002/anie.201510463.

[16]   A. Fujishima, K. Honda, Electrochemical Photolysis of Water at a Semiconductor Electrode, Nature. 238 (1972) 37–38. doi:10.1038/238037a0.

[17]   K. Maeda, K. Teramura, D. Lu, T. Takata, N. Saito, Y. Inoue, et al., Photocatalyst releasing hydrogen from water, Nature. 440 (2006) 295–295. doi:10.1038/440295a.

[18]   K. Maeda, K. Domen, Photocatalytic Water Splitting: Recent Progress and Future Challenges, J. Phys. Chem. Lett. 1 (2010) 2655–2661. doi:10.1021/jz1007966.

[19]   F.E. Osterloh, Boosting the Efficiency of Suspended Photocatalysts for Overall Water Splitting, J. Phys. Chem. Lett. 5 (2014) 2510–2511. doi:10.1021/jz501342j.

[20]   D.M. Fabian, S. Hu, N. Singh, F.A. Houle, T. Hisatomi, K. Domen, et al., Particle suspension reactors and materials for solar-driven water splitting, Energy Environ. Sci. 8 (2015) 2825–2850. doi:10.1039/C5EE01434D.

[21]   O. Khaselev, High-efficiency integrated multijunction photovoltaic/electrolysis systems for hydrogen production, Int. J. Hydrogen Energy. 26 (2001) 127–132. doi:10.1016/S0360-3199(00)00039-2.

[22]   S.Y. Reece, J.A. Hamel, K. Sung, T.D. Jarvi, A.J. Esswein, J.J.H. Pijpers, et al., Wireless Solar Water Splitting Using Silicon-Based Semiconductors and Earth-Abundant Catalysts, Science (80-.). 334 (2011) 645–648. doi:10.1126/science.1209816.

[23]   K. Walczak, Y. Chen, C. Karp, J.W. Beeman, M. Shaner, J. Spurgeon, et al., Modeling, Simulation, and Fabrication of a Fully Integrated, Acid-stable, Scalable Solar-Driven Water-Splitting System, ChemSusChem. 8 (2015) 544–551. doi:10.1002/cssc.201402896.

[24]   M.A. Modestino, K.A. Walczak, A. Berger, C.M. Evans, S. Haussener, C. Koval, et al., Robust production of purified H 2 in a stable, self-regulating, and continuously operating solar fuel generator, Energy Environ. Sci. 7 (2014) 297–301. doi:10.1039/C3EE43214A.

[25]   S. Licht, B. Wang, S. Mukerji, T. Soga, M. Umeno, H. Tributsch, Over 18% solar energy conversion to generation of hydrogen fuel; theory and experiment for efficient solar water splitting, Int. J. Hydrogen Energy. 26 (2001) 653–659. doi:10.1016/S0360-3199(00)00133-6.

[26]   J. Jia, L.C. Seitz, J.D. Benck, Y. Huo, Y. Chen, J.W.D. Ng, et al., Solar water splitting by photovoltaic-electrolysis with a solar-to-hydrogen efficiency over 30%, Nat. Commun. 7 (2016) 13237. doi:10.1038/ncomms13237.

[27]   S. Hu, C. Xiang, S. Haussener, A.D. Berger, N.S. Lewis, An analysis of the optimal band gaps of light absorbers in integrated tandem photoelectrochemical water-splitting systems, Energy Environ. Sci. 6 (2013) 2984. doi:10.1039/c3ee40453f.

[28]   S. Haussener, C. Xiang, J.M. Spurgeon, S. Ardo, N.S. Lewis, A.Z. Weber, Modeling, simulation, and design criteria for photoelectrochemical water-splitting systems, Energy Environ. Sci. 5 (2012) 9922. doi:10.1039/c2ee23187e.

[29]   S. Haussener, S. Hu, C. Xiang, A.Z. Weber, N.S. Lewis, Simulations of the irradiation and temperature dependence of the efficiency of tandem photoelectrochemical water-splitting systems, Energy Environ. Sci. 6 (2013) 3605. doi:10.1039/c3ee41302k.

[30]   C. Xiang, Y. Chen, N.S. Lewis, Modeling an integrated photoelectrolysis system sustained by water vapor, Energy Environ. Sci. 6 (2013) 3713. doi:10.1039/c3ee42143k.

[31]   M.R. Singh, K. Papadantonakis, C. Xiang, N.S. Lewis, An electrochemical engineering assessment of the operational conditions and constraints for solar-driven water-splitting systems at near-neutral pH, Energy Environ. Sci. 8 (2015) 2760–2767. doi:10.1039/C5EE01721A.

[32]   J.C. Stevens, A.Z. Weber, A Computational Study of Optically Concentrating, Solar-Fuels Generators from Annual Thermal- and Fuel-Production Efficiency Perspectives, J. Electrochem. Soc. 163 (2016) H475–H484. doi:10.1149/2.0121607jes.

[33]   Y. Surendranath, D.K. Bediako, D.G. Nocera, Interplay of oxygen-evolution kinetics and photovoltaic power curves on the construction of artificial leaves., Proc. Natl. Acad. Sci. U. S. A. 109 (2012) 15617–21. doi:10.1073/pnas.1118341109.

[34]   S. Tembhurne, S. Haussener, Integrated Photo-Electrochemical Solar Fuel Generators under Concentrated Irradiation, J. Electrochem. Soc. 163 (2016) H988–H998. doi:10.1149/2.0311610jes.

[35]   B.D. James, G.N. Baum, J. Perez, K.N. Baum, Technoeconomic Analysis of Photoelectrochemical (PEC) Hydrogen Production, Virginia, 2009. http://energy.gov/eere/fuelcells/downloads/technoeconomic-analysis-photoelectrochemical-pec-hydrogen-production.

[36]   B.A. Pinaud, J.D. Benck, L.C. Seitz, A.J. Forman, Z. Chen, T.G. Deutsch, et al., Technical and economic feasibility of centralized facilities for solar hydrogen production via photocatalysis and photoelectrochemistry, Energy Environ. Sci. 6 (2013) 1983. doi:10.1039/c3ee40831k.

[37]   M.R. Shaner, H.A. Atwater, N.S. Lewis, E.W. McFarland, A comparative technoeconomic analysis of renewable hydrogen production using solar energy, Energy Environ. Sci. 9 (2016) 2354–2371. doi:10.1039/C5EE02573G.

[38]   Q. Wang, T. Hisatomi, Q. Jia, H. Tokudome, M. Zhong, C. Wang, et al., Scalable water splitting on particulate photocatalyst sheets with a solar-to-hydrogen energy conversion efficiency exceeding 1%, Nat. Mater. 15 (2016) 611–615. doi:10.1038/nmat4589.

[39]   Q. Wang, T. Hisatomi, Y. Suzuki, Z. Pan, J. Seo, M. Katayama, et al., Particulate Photocatalyst Sheets Based on Carbon Conductor Layer for Efficient Z-Scheme Pure-Water Splitting at Ambient Pressure, J. Am. Chem. Soc. 139 (2017) 1675–1683. doi:10.1021/jacs.6b12164.

[40]   K. Sayama, K. Mukasa, R. Abe, Y. Abe, H. Arakawa, Stoichiometric water splitting into H_2 and O_2 using a mixture of two different photocatalysts and an IO3−/I− shuttle redox mediator under visible light irradiation, Chem. Commun. 0 (2001) 2416–2417. doi:10.1039/b107673f.

[41]   Y. Miseki, S. Fujiyoshi, T. Gunji, K. Sayama, Photocatalytic water splitting under visible light utilizing I3−/I− and IO3−/I− redox mediators by Z-scheme system using surface treated PtOx/WO3 as O2 evolution photocatalyst, Catal. Sci. Technol. 3 (2013) 1750. doi:10.1039/c3cy00055a.

[42]   R. Abe, T. Takata, H. Sugihara, K. Domen, Photocatalytic overall water splitting

under visible light by TaON and WO3 with an IO3-/I- shuttle redox mediator., Chem. Commun. (Camb). (2005) 3829–31. doi:10.1039/b505646b.

[43]   K. Maeda, M. Higashi, D. Lu, R. Abe, K. Domen, Efficient nonsacrificial water splitting through two-step photoexcitation by visible light using a modified oxynitride as a hydrogen evolution photocatalyst., J. Am. Chem. Soc. 132 (2010) 5858–68. doi:10.1021/ja1009025.

[44]   S.-C. Yu, C.-W. Huang, C.-H. Liao, J.C.S. Wu, S.-T. Chang, K.-H. Chen, A novel membrane reactor for separating hydrogen and oxygen in photocatalytic water splitting, J. Memb. Sci. 382 (2011) 291–299. doi:10.1016/j.memsci.2011.08.022.

[45]   C.-C. Lo, C.-W. Huang, C.-H. Liao, J.C.S. Wu, Novel twin reactor for separate evolution of hydrogen and oxygen in photocatalytic water splitting, Int. J. Hydrogen Energy. 35 (2010) 1523–1529. doi:10.1016/j.ijhydene.2009.12.032.

[46]   K. Maeda, Rhodium-Doped Barium Titanate Perovskite as a Stable p-Type Semiconductor Photocatalyst for Hydrogen Evolution under Visible Light, ACS Appl. Mater. Interfaces. 6 (2014) 2167–2173. doi:10.1021/am405293e.

[47]   H. Suzuki, O. Tomita, M. Higashi, R. Abe, Two-step photocatalytic water splitting into H 2 and O 2 using layered metal oxide KCa2 Nb 3 O 10 and its derivatives as O2 -evolving photocatalysts with IO 3 − /I − or Fe 3+ /Fe 2+ redox mediator, Catal. Sci. Technol. 5 (2015) 2640–2648. doi:10.1039/C5CY00128E.

[48]   H. Kato, Y. Sasaki, N. Shirakura, A. Kudo, Synthesis of highly active rhodium-doped SrTiO$_3$ powders in Z-scheme systems for visible-light-driven photocatalytic overall water splitting, J. Mater. Chem. A. 1 (2013) 12327. doi:10.1039/c3ta12803b.

[49]   R. Abe, K. Sayama, H. Arakawa, Significant effect of iodide addition on water splitting into H2 and O2 over Pt-loaded TiO2 photocatalyst: suppression of backward reaction, Chem. Phys. Lett. 371 (2003) 360–364. doi:10.1016/S0009-2614(03)00252-5.

[50]   Y. Sasaki, A. Iwase, H. Kato, A. Kudo, The effect of co-catalyst for Z-scheme photocatalysis systems with an Fe3+/Fe2+ electron mediator on overall water splitting under visible light irradiation, J. Catal. 259 (2008) 133–137. doi:10.1016/j.jcat.2008.07.017.

[51]   Q. Wang, T. Hisatomi, S.S.K. Ma, Y. Li, K. Domen, Core/Shell Structured La- and Rh-Codoped SrTiO$_3$ as a Hydrogen Evolution Photocatalyst in Z-Scheme Overall Water Splitting under Visible Light Irradiation, Chem. Mater. 26 (2014) 4144–4150. doi:10.1021/cm5011983.

[52]   R.R. Jaini, T.F. Fuller, Overcoming mass-transfer limitations in the Dual Bed Colloidal Suspension Reactor, Int. J. Hydrogen Energy. 39 (2014) 2462–2471. doi:10.1016/j.ijhydene.2013.12.018.

[53]   R.J. Brandi, O.M. Alfano, A.E. Cassano, Evaluation of Radiation Absorption in Slurry Photocatalytic Reactors. 1. Assessment of Methods in Use and New Proposal, Environ. Sci. Technol. 34 (2000) 2623–2630. doi:10.1021/es9909428.

[54]   A. Busciglio, O.M. Alfano, F. Scargiali, A. Brucato, A probabilistic approach to radiant field modeling in dense particulate systems, Chem. Eng. Sci. 142 (2015) 79–88. doi:10.1016/j.ces.2015.11.025.

[55]   M.L. Satuf, R.J. Brandi, A.E. Cassano, O.M. Alfano, Experimental Method to Evaluate the Optical Properties of Aqueous Titanium Dioxide Suspensions, Ind.

Eng. Chem. Res. 44 (2005) 6643–6649. doi:10.1021/ie050365y.

[56]   M. de los M. Ballari, R. Brandi, O. Alfano, A. Cassano, Mass transfer limitations in photocatalytic reactors employing titanium dioxide suspensions: II. External and internal particle constrains for the reaction, Chem. Eng. J. 136 (2008) 242–255. doi:10.1016/j.cej.2007.03.031.

[57]   A.E. Cassano, O.M. Alfano, Reaction engineering of suspended solid heterogeneous photocatalytic reactors, Catal. Today. 58 (2000) 167–197. doi:10.1016/S0920-5861(00)00251-0.

[58]   H. Li, W. Tu, Y. Zhou, Z. Zou, Z-Scheme Photocatalytic Systems for Promoting Photocatalytic Performance: Recent Progress and Future Challenges, Adv. Sci. (2016). doi:10.1002/advs.201500389.

[59]   R.M. Navarro, F. del Valle, J.A. Villoria de la Mano, M.C. Álvarez-Galván, J.L.G. Fierro, Advances in Chemical Engineering - Photocatalytic Technologies, Elsevier, 2009. doi:10.1016/S0065-2377(09)00404-9.

[60]   Y. Xu, M.A.A. Schoonen, The absolute energy positions of conduction and valence bands of selected semiconducting minerals, Am. Mineral. 85 (2000) 543–556. doi:10.2138/am-2000-0416.

[61]   Y. Park, K.J. McDonald, K.-S. Choi, Progress in bismuth vanadate photoanodes for use in solar water oxidation, Chem. Soc. Rev. 42 (2013) 2321–2337. doi:10.1039/C2CS35260E.

[62]   R. Asai, H. Nemoto, Q. Jia, K. Saito, A. Iwase, A. Kudo, A visible light responsive rhodium and antimony-codoped $SrTiO_3$ powdered photocatalyst loaded with an IrO_2 cocatalyst for solar water splitting, Chem. Commun. 50 (2014) 2543. doi:10.1039/c3cc49279f.

[63]   Y. Miseki, H. Kusama, H. Sugihara, K. Sayama, Cs-Modified WO_3 Photocatalyst Showing Efficient Solar Energy Conversion for O_2 Production and Fe (III) Ion Reduction under Visible Light, J. Phys. Chem. Lett. 1 (2010) 1196–1200. doi:10.1021/jz100233w.

[64]   B. Huskinson, M.P. Marshak, C. Suh, S. Er, M.R. Gerhardt, C.J. Galvin, et al., A metal-free organic–inorganic aqueous flow battery, Nature. 505 (2014) 195–198. doi:10.1038/nature12909.

[65]   B. Yang, L. Hoober-Burkhardt, F. Wang, G.K. Surya Prakash, S.R. Narayanan, An Inexpensive Aqueous Flow Battery for Large-Scale Electrical Energy Storage Based on Water-Soluble Organic Redox Couples, J. Electrochem. Soc. 161 (2014) A1371–A1380. doi:10.1149/2.1001409jes.

[66]   K. Lin, Q. Chen, M.R. Gerhardt, L. Tong, S.B. Kim, L. Eisenach, et al., Alkaline quinone flow battery, Science (80-.). 349 (2015). http://science.sciencemag.org/content/349/6255/1529 (accessed April 16, 2017).

[67]   G. Lodi, E. Sivieri, A. De Battisti, S. Trasatti, Ruthenium dioxide-based film electrodes, J. Appl. Electrochem. 8 (1978) 135–143. doi:10.1007/BF00617671.

[68]   C.C.L. McCrory, S. Jung, J.C. Peters, T.F. Jaramillo, Benchmarking Heterogeneous Electrocatalysts for the Oxygen Evolution Reaction, J. Am. Chem. Soc. 135 (2013) 16977–16987. doi:10.1021/ja407115p.

[69]   S. Trasatti, Work function, electronegativity, and electrochemical behaviour of metals, J. Electroanal. Chem. Interfacial Electrochem. 39 (1972) 163–184. doi:10.1016/S0022-0728(72)80485-6.

[70]   C.C.L. McCrory, S. Jung, I.M. Ferrer, S. Chatman, J.C. Peters, T.F. Jaramillo, Benchmarking HER and OER Electrocatalysts for Solar Water Splitting Devices., J. Am. Chem. Soc. 137 (2015) 4347–4357. doi:10.1021/ja510442p.

[71]   S. Xie, Q. Zhang, G. Liu, Y. Wang, Photocatalytic and photoelectrocatalytic reduction of CO 2 using heterogeneous catalysts with controlled nanostructures, Chem. Commun. 52 (2016) 35–59. doi:10.1039/C5CC07613G.

[72]   S. Kawasaki, K. Akagi, K. Nakatsuji, S. Yamamoto, I. Matsuda, Y. Harada, et al., Elucidation of Rh-Induced In-Gap States of Rh:SrTiO 3 Visible-Light-Driven Photocatalyst by Soft X-ray Spectroscopy and First-Principles Calculations, J. Phys. Chem. C. 116 (2012) 24445–24448. doi:10.1021/jp3082529.

[73]   B. Modak, S.K. Ghosh, Enhancement of Visible Light Photocatalytic Activity of SrTiO 3 : A Hybrid Density Functional Study, J. Phys. Chem. C. 119 (2015) 23503–23514. doi:10.1021/acs.jpcc.5b06667.

[74]   D. Perrin, Dissociation constants of organic bases in aqueous solution, Butterworths, London, 1972. http://www.worldcat.org/title/dissociation-constants-of-organic-bases-in-aqueous-solution/oclc/878462380?referer=null&ht=edition (accessed July 27, 2017).

[75]   E.P. Serjeant, B. Dempsey, Ionisation constants of organic acids in aqueous solution, Pergamon Press, Oxford;New York, 1979. http://www.worldcat.org/title/ionisation-constants-of-organic-acids-in-aqueous-solution/oclc/4494248 (accessed July 27, 2017).

[76]   M.F. Modest, The Radiative Transfer Equation in Participating Media(RTE), in: Radiat. Heat Transf., Second, Academic Press, 2003: pp. 279–302.

[77]   J. Newman, K.E. Thomas-Alyea, Infinitely Dilute Solutions, in: Electrochem. Syst., Third, John Wiley & Sons, Inc., Hoboken, NJ, USA, 2004: pp. 271–289.

[78]   W.M. Haynes, Thermo, Electro and Solution Chemistry, in: Handb. Chem. Phys., 94th ed., Baca Raton, n.d.

[79]   A.J. Bard, L.R. Faulkner, Electrochemical Methods Fundamentals and Applications, John Wiley & Sons, Inc., 2001.

[80]   ASTM, Reference Solar Spectral Irradiance : Air Mass 1.5, (n.d.). http://rredc.nrel.gov/solar/spectra/am1.5/.

[81]   NREL, National Solar Radiation Data Base, 1991- 2005 Update: Typical Meteorological Year 3, (n.d.). http://rredc.nrel.gov/solar/old_data/nsrdb/1991-2005/tmy3/.

[82]   G.M. Hale, M.R. Querry, Optical Constants of Water in the 200-nm to 200-μm Wavelength Region, Appl. Opt. 12 (1973) 555. doi:10.1364/AO.12.000555.

[83]   M.I. Cabrera, O.M. Alfano, A.E. Cassano, Absorption and Scattering Coefficients of Titanium Dioxide Particulate Suspensions in Water, J. Phys. Chem. 100 (1996) 20043–20050. doi:10.1021/jp962095q.

[84]   V. Sivakumar, R. Suresh, K. Giribabu, V. Narayanan, BiVO 4 nanoparticles: Preparation, characterization and photocatalytic activity, Cogent Chem. 1 (2015) 1074647. doi:10.1080/23312009.2015.1074647.

[85]   R.O. Rahn, M.I. Stefan, J.R. Bolton, E. Goren, P.-S. Shaw, K.R. Lykke, Quantum yield of the iodide-iodate chemical actinometer: dependence on wavelength and concentrations., Photochem. Photobiol. 78 (2003) 146–52. http://www.ncbi.nlm.nih.gov/pubmed/12945582 (accessed June 29, 2016).

[86]   M. Huwiler, H. Kohler, Pseudo-catalytic degradation of hydrogen peroxide in the lactoperoxidase/H_2O_2/iodide system, Eur. J. Biochem. 141 (1984) 69–74. doi:10.1111/j.1432-1033.1984.tb08158.x.

[87]   V. Talrose, A.N. Yermakov, A.A. Usov, A.A. Goncharova, A.N. Leskin, N.A. Messineva, et al., UV/Visible Spectra, in: P.J. Linstrom, W.G. Mallard (Eds.), NIST Chem. WebBook, NIST Stand. Ref. Database Number 69, Gaithersburg, n.d. http://webbook.nist.gov.

[88]   M.R. Shaner, K.T. Fountaine, H.-J. Lewerenz, Current-voltage characteristics of coupled photodiode-electrocatalyst devices, Appl. Phys. Lett. 103 (2013) 143905. doi:10.1063/1.4822179.

[89]   M.X. Tan, P.E. Laibinis, S.T. Nguyen, J.M. Kesselman, C.E. Stanton, N.S. Lewis, Principles and Applications of Semiconductor Photoelectrochemistry, in: K.D. Karlin (Ed.), Prog. Inorg. Chem. Vol. 41, John Wiley & Sons, Inc., Hoboken, 1984: pp. 21–144. doi:10.1002/9780470166420.ch2.

[90]   J. Newman, K.E. Thomas-Alyea, Electrode Kinetics, in: Electrochem. Syst., Third, John Wiley & Sons, Inc., Hoboken, NJ, USA, 2004: pp. 203–230.

[91]   Comsol Inc., Comsol Multiphysics 5.2, (2015).

[92]   M. Grätzel, U. Bach, D. Lupo, P. Comte, J.E. Moser, F. Weissörtel, et al., Solid-state dye-sensitized mesoporous TiO2 solar cells with high photon-to-electron conversion efficiencies, Nature. 395 (1998) 583–585. doi:10.1038/26936.

[93]   A. Kay, I. Cesar, M. Grätzel, New Benchmark for Water Photooxidation by Nanostructured α-Fe 2 O 3 Films, J. Am. Chem. Soc. 128 (2006) 15714–15721. doi:10.1021/ja064380l.

[94]   J.M. Spurgeon, M.G. Walter, J. Zhou, P.A. Kohl, N.S. Lewis, E.L. Warren, et al., Electrical conductivity, ionic conductivity, optical absorption, and gas separation properties of ionically conductive polymer membranes embedded with Si microwire arrays, Energy Environ. Sci. 4 (2011) 1772. doi:10.1039/c1ee01028j.

[95]   E.L. Warren, S.W. Boettcher, M.G. Walter, H.A. Atwater, N.S. Lewis, pH-Independent, 520 mV Open-Circuit Voltages of Si/Methyl Viologen [2+/+] Contacts Through Use of Radial n [+] p-Si Junction Microwire Array Photoelectrodes, J. Phys. Chem. C. 115 (2011) 594–598. doi:10.1021/jp109147p.

[96]   C. Liu, J. Tang, H.M. Chen, B. Liu, P. Yang, A Fully Integrated Nanosystem of Semiconductor Nanowires for Direct Solar Water Splitting, Nano Lett. 13 (2013) 2989–2992. doi:10.1021/nl401615t.

[97]   D. V. Esposito, Y. Lee, H. Yoon, P.M. Haney, N.Y. Labrador, T.P. Moffat, et al., Deconvoluting the influences of 3D structure on the performance of photoelectrodes for solar-driven water splitting, Sustain. Energy Fuels. 1 (2017) 154–173. doi:10.1039/C6SE00073H.